Local and Mesoscale Impacts of Wind Farms as Parameterized in a Mesoscale NWP Model

ANNA C. FITCH,* JOSEPH B. OLSON,+ JULIE K. LUNDQUIST,# JIMY DUDHIA,@ ALOK K. GUPTA,& JOHN MICHALAKES,** AND IDAR BARSTAD&

* *Geophysical Institute, University of Bergen, and Uni Research, Bergen, Norway, and Mesoscale and Microscale Meteorology Division, National Center for Atmospheric Research, Boulder, Colorado*
+ *NOAA/Earth System Research Laboratory, and Cooperative Institute for Research in Environmental Sciences, Boulder, Colorado*
# *Department of Atmospheric and Oceanic Sciences, University of Colorado, Boulder, and National Renewable Energy Laboratory, Golden, Colorado*
@ *Mesoscale and Microscale Meteorology Division, National Center for Atmospheric Research, Boulder, Colorado*
& *Uni Research, Bergen, Norway*
** *National Renewable Energy Laboratory, Golden, Colorado*

(Manuscript received 3 December 2011, in final form 15 February 2012)

ABSTRACT

A new wind farm parameterization has been developed for the mesoscale numerical weather prediction model, the Weather Research and Forecasting model (WRF). The effects of wind turbines are represented by imposing a momentum sink on the mean flow; transferring kinetic energy into electricity and turbulent kinetic energy (TKE). The parameterization improves upon previous models, basing the atmospheric drag of turbines on the thrust coefficient of a modern commercial turbine. In addition, the source of TKE varies with wind speed, reflecting the amount of energy extracted from the atmosphere by the turbines that does not produce electrical energy.

Analyses of idealized simulations of a large offshore wind farm are presented to highlight the perturbation induced by the wind farm and its interaction with the atmospheric boundary layer (BL). A wind speed deficit extended throughout the depth of the neutral boundary layer, above and downstream from the farm, with a long wake of 60-km *e*-folding distance. Within the farm the wind speed deficit reached a maximum reduction of 16%. A maximum increase of TKE, by nearly a factor of 7, was located within the farm. The increase in TKE extended to the top of the BL above the farm due to vertical transport and wind shear, significantly enhancing turbulent momentum fluxes. The TKE increased by a factor of 2 near the surface within the farm. Near-surface winds accelerated by up to 11%. These results are consistent with the few results available from observations and large-eddy simulations, indicating this parameterization provides a reasonable means of exploring potential downwind impacts of large wind farms.

1. Introduction

Wind energy has become the fastest-growing renewable energy resource worldwide, with wind farms in development covering increasingly large areas. Greater understanding of the interaction between the atmospheric boundary layer (BL) and wind turbines is necessary to ensure energy production and the lifetime of turbines are maximized. In addition, questions are emerging over the potential impacts of wind farms on meteorology, and their ability to affect downwind agriculture and other economic activities.

Few observational reports quantify the impact of large wind farms on local wind, turbulence, temperature, or moisture flux. Wakes from offshore wind farms have been observed using satellite synthetic aperture radar (SAR) by Christiansen and Hasager (2005). Within 1–2 km downstream of the Horns Rev and Nysted wind farms in Denmark, an average wind speed deficit of 8%–9% was found, corresponding to an absolute reduction of 0.5–1.5 m s^{-1}. The wake recovery depended

Corresponding author address: Anna C. Fitch, Mesoscale and Microscale Meteorology Division, National Center for Atmospheric Research, P.O. Box 3000, Boulder, CO 80307.
E-mail: anna.fitch@gfi.uib.no

DOI: 10.1175/MWR-D-11-00352.1

on not only the ambient wind speed, but also atmospheric stability and the number of turbines in operation. In unstable cases, the wind speed recovered to within 2% of the upstream velocity, over a distance of 5 km. For neutral cases, however, at least a 2% deficit persisted over the distance investigated (21 km). Turbulence intensity was increased downwind of the wind farms in around a third of the cases studied.

In addition to impacts on winds and turbulence, wind farms may influence temperature downwind. Baidya Roy and Traiteur (2010) considered observations from the San Gorgonio wind farm, consisting of 1000 turbines of nominal power 44–108 kW, with hub heights of 23 m. Their analysis suggested the wind farm modified near-surface air temperatures within and downwind of the farm. The sign of the temperature change depended on the stratification of the low-level air, with a stable stratification leading to a warming and an unstable stratification leading to a cooling. Such temperature shifts, if they occurred over a growing season, could impact the viability of some crops grown near and downstream of wind farms.

Despite the importance of the atmospheric impacts of large wind farms, few observations, other than those summarized above, exist and so inquiries into wind farm impacts continue in the modeling domain. A variety of different approaches to parameterize the effects of wind farms have been employed: 1) direct explicit parameterization of individual turbine drag on local flows within a computational fluid dynamics or large-eddy simulation (LES) domain, 2) explicit treatment of elevated drag and turbulent mixing to represent aggregation of several turbines within regional or mesoscale models, and 3) implicit parameterization through enlarged surface aerodynamic roughness length to represent the general impacts of wind farms on synoptic or global scales.

The first, or *bottom-up* approach, focuses on the interaction of individual turbines with the atmosphere and the impact on surrounding turbines. This approach is an important complement to observational studies, which have difficulty sampling the complete four-dimensional impacts of wind farms on the environment. Results from this approach may be used to help guide the development of parameterizations of type 2) or 3). Calaf et al. (2010) quantified the vertical transport of momentum and kinetic energy (KE) associated with large wind farms using LES, representing turbines using the drag-disk concept. Vertical fluxes of kinetic energy (KE) were of the same order of magnitude as the power extracted by the wind turbines. Lu and Porté-Agel (2011) simulated an infinitely large wind farm by modeling a single wind turbine using an actuator line technique in a three-dimensional (3D) LES domain with periodic boundaries. The height of the shallow (175 m) boundary layer increased, as did the temperature within the rotor area, owing to induced mixing by the turbine. Conversely, the wind farm reduced turbulent mixing and transport near the surface. Furthermore, turbulence intensity increased above hub height, and was transported away from the center of the wake owing to the turning of the wind in the Ekman spiral. Finally, in a wind-tunnel experiment with a 3×3 array of model wind turbines, Cal et al. (2011) confirmed that fluxes of KE associated with Reynolds shear stresses were of the same order of magnitude as the energy extracted by the wind turbines. At these scales, the generation of turbulent kinetic energy (TKE) by a wind farm must either be resolved or treated explicitly.

At coarser regional and global scales, wind farms have been represented by approaches 2) or 3). The latter approach represents wind farms with increased surface roughness, similar to a large forest (Ivanova and Nadyozhina 2000; Keith et al. 2004; Kirk-Davidoff and Keith 2008; Barrie and Kirk-Davidoff 2010; Wang and Prinn 2010, 2011). In the absence of field measurements, it is difficult to choose an appropriate roughness length scale. Furthermore, this approach does not enable insight into the details of the vertical wind profile in the lowest 200 m where impacts on turbulent stresses are important. However, because this approach is computationally efficient, estimates of large-scale impacts of wind farms with thousands of turbines have been attempted within global climate models. Kirk-Davidoff and Keith (2008) found surface roughness anomalies covering large areas representing wind farms generated appreciable wind, temperature, and cloudiness anomalies. Barrie and Kirk-Davidoff (2010) showed the initial disturbance generated by a large wind farm induced a synoptic response. With a coupled atmosphere–ocean climate model, Wang and Prinn (2010) represented wind farms by modifying surface roughness and displacement height. They found temperatures warmed by 1°C over onshore wind farms and cooled by 1°C over offshore wind farms, with the warming limited to the lowermost layers in the atmosphere. Ocean–atmosphere heat fluxes increased in response to increased turbulence.

The intermediate approach (i.e., 2), typically employed with mesoscale or limited-area models, represents a wind farm as an elevated momentum sink and a source of turbulence (TKE), as in Baidya Roy et al. (2004), Adams and Keith (2007), Baidya Roy and Traiteur (2010), Blahak et al. (2010), and Baidya Roy (2011). These approaches are distinguished by their means of quantifying the momentum sink and the TKE

produced by a wind farm, with varying degrees of fidelity to turbine operations. Baidya Roy et al. (2004) calculated the amount of KE flowing through the rotor blades, and removed a fraction equal to the power coefficient C_P to represent energy converted into electrical energy by the turbines. They chose a constant value of $C_P = 0.4$, while in practice, C_P varies with wind speed. A constant value of TKE was added to the background TKE to represent turbulence generated by the turbines. The resolved KE of the flow was reduced by a corresponding amount to conserve energy. Baidya Roy (2011) enhanced their previous model, basing the fraction of energy extracted from the flow by the turbines on the power coefficient of a commercial wind turbine. Blahak et al. (2010) used a similar approach, but instead of extracting a fraction of energy from the atmosphere based on only the power coefficient, they added a loss factor to include mechanical and electrical losses in the turbines. The fraction of energy converted to TKE was still constant with wind speed, however.

This type of modeling approach produces impacts similar to those observed with LES and in wind tunnels. Baidya Roy et al. (2004) showed the wind at the hub-height level of the turbines slowed significantly, and turbulence generated by the turbines enhanced vertical mixing of momentum and heat. Under stable stratification, their results showed a warming of the surface and cooling of the surface with unstable stratification. When the source of TKE from the turbines was increased, the impacts on near-surface air temperatures were greater. The downwind impacts of the farm appeared to persist only 18–23 km from the downwind edge of the farm regardless of the wind farm size (Baidya Roy 2011).

The wind farm parameterization developed here improves upon previous mesoscale simulations by representing turbine drag using the thrust coefficient data from a modern commercial turbine. In addition, the TKE produced is reflective of wind speed, as described in section 2. This wind farm parameterization is implemented in the Weather Research and Forecasting model (WRF; Skamarock et al. 2008) and is included in the WRF 3.3 distribution of April 2011 (Dudhia 2011). To explore the performance of the parameterization, we design an idealized offshore wind farm consisting of 10×10 turbines (discussed in section 3d), similar to the scale of the Thanet Offshore Wind Farm (see online at http://www.vattenfall.co.uk/en/thanet-offshore-wind-farm.htm), currently the largest offshore wind farm in the world. Effects of the wind farm on wind velocity, turbulent mixing, and momentum fluxes are discussed in section 4.

2. Wind farm parameterization

We expand the method of Blahak et al. (2010) by modeling the drag of turbines based on the total fraction of KE extracted from the atmosphere due to wind turbines, as quantified by the thrust coefficient C_T. The thrust coefficient is a function of wind speed and is dependent on the type of turbine. From the total KE extracted from the atmosphere, a fraction is converted into electrical energy, given by the power coefficient C_P. This coefficient depends on wind speed, and varies between 17%–75% of C_T for the turbines modeled here. The thrust and power coefficients can be obtained from the turbine manufacturer. The remaining energy extracted from the atmosphere that is not converted into useful electrical energy is consumed by mechanical and electrical losses, as well as nonproductive drag. Here we assume the mechanical and electrical losses are negligible, and that all the nonproductive drag of the turbine blades produces turbulence (TKE). The fraction of energy converted into TKE C_{TKE} is then given by $C_T - C_P$.

The force of drag induced by a wind turbine on the impinging flow can be represented by the drag equation:

$$\mathbf{F}_{\mathrm{drag}} = \frac{1}{2} C_T(|\mathbf{V}|)\rho|\mathbf{V}|\mathbf{V}A, \tag{1}$$

where $\mathbf{V} = (u, v)$ is the horizontal velocity vector (for the moment assumed to be uniform over the rotor area), C_T is the turbine thrust coefficient (assumed to be independent of air density), ρ is the air density, and $A = (\pi/4)D^2$ is the cross-sectional rotor area (where D is the diameter of the turbine blades). It is assumed the turbines are oriented perpendicular to the flow, which is typically the case of most modern large turbines. The drag of the turbine blades is assumed not to affect the vertical velocity component w. The drag of the wind turbine pole is neglected.

The rate of loss of KE from the atmosphere due to one wind turbine is then

$$\frac{\partial \mathrm{KE}_{\mathrm{drag}}}{\partial t} = -\frac{1}{2} C_T(|\mathbf{V}|)\rho|\mathbf{V}|^3 A. \tag{2}$$

The vertical profile of the horizontal wind is generally nonuniform, and should be integrated over the rotor area. Equation (2) becomes

$$\frac{\partial \mathrm{KE}_{\mathrm{drag}}}{\partial t} = -\frac{1}{2}\int_{A_R} C_T(|\mathbf{V}|)\rho|\mathbf{V}|^3 \, dA. \tag{3}$$

In a mesoscale model, the horizontal grid spacing may be greater than the distance between two wind turbines, and hence more than one wind turbine can be located in a model grid cell. To account for this, a horizontal density of wind turbines is defined (number of turbines per square meter) by N_t^{ij}, where i and j are the indices of the model grid cell in the zonal and meridional directions, respectively. The force of drag of the wind turbines in a grid cell can then be obtained by integrating over the horizontal area of the grid cell. Equation (3) becomes

$$\frac{\partial \mathrm{KE}_{\mathrm{drag}}^{ij}}{\partial t} = -\frac{1}{2}\int_{\Delta x}\int_{\Delta y} N_t^{ij}\left[\int_{A_R} C_T(|\mathbf{V}|)\rho|\mathbf{V}|^3\, dA\right] dy\, dx$$
$$= -\frac{1}{2}N_t^{ij}\Delta x\Delta y\left[\int_{A_R} C_T(|\mathbf{V}|)\rho|\mathbf{V}|^3\, dA\right], \quad (4)$$

where Δx, Δy is the horizontal grid size in the zonal and meridional directions, respectively. This model does not account for wake effects between turbines in one grid cell; only between turbines in adjacent grid cells.

The integral on the right-hand side (rhs) of Eq. (4) can be rewritten in terms of model grid indices i, j, k corresponding to the Cartesian coordinate directions x, y, z. The drag force is only applied to model levels containing turbine blades.

The rate of loss of KE in grid cell i, j and model level k is then

$$\frac{\partial \mathrm{KE}_{\mathrm{drag}}^{ijk}}{\partial t} = -\frac{1}{2}N_t^{ij}\Delta x\Delta y C_T(|\mathbf{V}|_{ijk})\rho_{ijk}|\mathbf{V}|_{ijk}^3 A_{ijk}, \quad (5)$$

where A_{ijk} is the cross-sectional rotor area of one wind turbine bounded by model levels k, $k + 1$ in grid cell i, j.

The kinetic energy loss due to wind turbines in grid cell i, j, k must be taken from the total KE in that grid cell. The total rate of change of KE in one grid cell is

$$\frac{\partial \mathrm{KE}_{\mathrm{cell}}^{ijk}}{\partial t} = \frac{\partial}{\partial t}\int_{\Delta x}\int_{\Delta y}\int_{\Delta z}\frac{\rho_{ijk}}{2}(u_{ijk}^2 + v_{ijk}^2 + w_{ijk}^2)\, dz\, dy\, dx, \quad (6)$$

where $\Delta z = z_{k+1} - z_k$, with z_k the height at model level k.

Only the horizontal wind component $\mathbf{V} = (u, v)$ is assumed to be affected by wind turbine drag. Equation (6) then becomes

$$\frac{\partial \mathrm{KE}_{\mathrm{cell}}^{ijk}}{\partial t} = \frac{\partial}{\partial t}\frac{\rho_{ijk}|\mathbf{V}|_{ijk}^2}{2}(z_{k+1} - z_k)\Delta x\Delta y$$
$$= \rho_{ijk}|\mathbf{V}|_{ijk}\frac{\partial|\mathbf{V}|_{ijk}}{\partial t}(z_{k+1} - z_k)\Delta x\Delta y. \quad (7)$$

The rate of change of KE within grid cell i, j, k is equal to the rate of loss of KE due to wind turbines in that cell. Equating Eqs. (5) and (7) results in the momentum tendency term:

$$\frac{\partial|\mathbf{V}|_{ijk}}{\partial t} = -\frac{\frac{1}{2}N_t^{ij}C_T(|\mathbf{V}|_{ijk})|\mathbf{V}|_{ijk}^2 A_{ijk}}{(z_{k+1} - z_k)}. \quad (8)$$

This equation can be expressed in component form, giving the horizontal momentum tendency terms, which can be applied in the model:

$$\frac{\partial u_{ijk}}{\partial t} = \frac{u_{ijk}}{|\mathbf{V}|_{ijk}}\frac{\partial|\mathbf{V}|_{ijk}}{\partial t}, \quad (9)$$

$$\frac{\partial v_{ijk}}{\partial t} = \frac{v_{ijk}}{|\mathbf{V}|_{ijk}}\frac{\partial|\mathbf{V}|_{ijk}}{\partial t}. \quad (10)$$

The power extracted by the turbines, which is converted into useful electrical energy, is given by

$$\frac{\partial P_{ijk}}{\partial t} = \frac{\frac{1}{2}N_t^{ij}C_P(|\mathbf{V}|_{ijk})|\mathbf{V}|_{ijk}^3 A_{ijk}}{(z_{k+1} - z_k)}. \quad (11)$$

The power extracted by the turbines, which is not converted into electricity, is converted into TKE:

$$\frac{\partial \mathrm{TKE}_{ijk}}{\partial t} = \frac{\frac{1}{2}N_t^{ij}C_{\mathrm{TKE}}(|\mathbf{V}|_{ijk})|\mathbf{V}|_{ijk}^3 A_{ijk}}{(z_{k+1} - z_k)}. \quad (12)$$

Therefore, the wind farm parameterization represents the effects of the turbines on the atmosphere by imposing a momentum sink on the mean flow, transferring a fraction of the KE into electricity, and the rest into TKE. With this approach, it is assumed that the TKE source represents the stirring of the ambient flow by the turbines, but not the mixing that results from the vertical wind shear induced by the momentum sink. This latter mixing is produced by the PBL scheme, as described in section 3b.

3. Experimental method

a. Model configuration

The mesoscale numerical weather prediction model, the Advanced Research WRF (ARW; version 3.3;

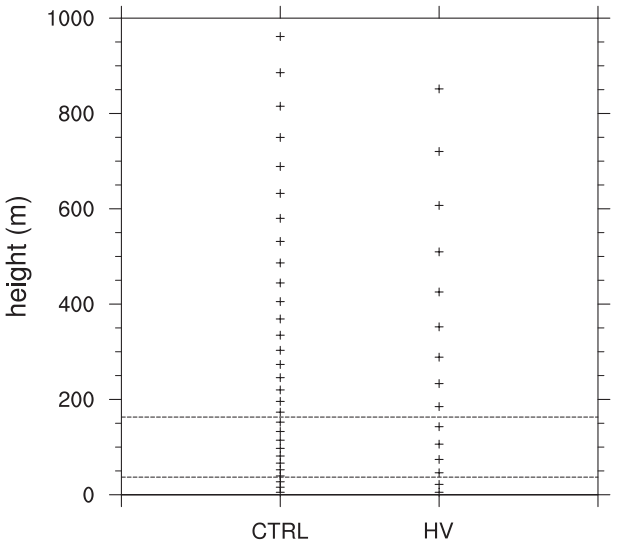

FIG. 1. Distribution of model midpoint levels with height in the boundary layer, for the control simulation (CTRL), and half vertical resolution simulation (HV). The horizontal lines indicate the rotor area.

Skamarock et al. 2008) is used to perform a series of idealized simulations to investigate the interaction of a large offshore wind farm with the boundary layer. ARW solves the nonhydrostatic compressible Euler equations discretized on an Arakawa-C staggered grid. A terrain-following hydrostatic pressure coordinate is used, with the grid stretched in the vertical and uniform grid spacing in the horizontal. A fifth-order finite-difference scheme is used for advection in the horizontal and a third-order scheme in the vertical. Time integration is handled by a third-order Runge–Kutta scheme.

The model is used with a two-way nested grid configuration, where the fine grid solution replaces the coarse grid solution for every coarse grid point inside the fine grid. Both grids have dimensions of 202 × 202 points, with 3- and 1-km horizontal resolution for the coarse and fine grids, respectively. The fine grid is centered inside the coarse grid. In the vertical there are 81 levels, with 30 levels below 1 km and 8 levels intersecting the rotor area (Fig. 1). The model top is at 20 km. The time step is 9 and 3 s for the coarse and fine grids, respectively. Both domains have a uniformly flat surface, with the surface pressure set to 1000 hPa. An f plane is used, with the Coriolis parameter set to a typical midlatitude value of 10^{-4} s^{-1}.

Open radiative lateral boundary conditions are used on all boundaries of the coarse grid, following the method of Klemp and Wilhelmson (1978). For the fine grid, the boundary conditions are interpolated from the coarse grid at the outermost rows and columns of the fine grid. At the upper boundary, a Rayleigh relaxation layer, of depth 5 km, controls reflection.

b. Model physics

The WRF model physics are configured to isolate the turbulent mixing induced by the wind farm. Surface heat and moisture fluxes and the radiation scheme are turned off, and the atmosphere is dry. Subgrid-scale turbulent mixing in the horizontal is represented by a second-order diffusion scheme, using eddy viscosities computed from the horizontal deformation. The bottom boundary is defined as a sea surface, with the roughness length given by the Charnock relation (Charnock 1955), plus a smooth sea surface limit, following Smith (1988).

Planetary boundary layer (PBL) physics is parameterized using the Mellor–Yamada–Nakanishi–Niino (MYNN) model (Nakanishi and Niino 2009). The MYNN model builds upon the Mellor–Yamada turbulence closure model (Mellor and Yamada 1974, 1982) to include the effects of stability on the mixing length scale, as well as the effects of buoyancy on pressure covariances. LES was employed by Nakanishi and Niino (2009) to determine the fundamental closure constants. In addition, the prediction of TKE was tuned to match LES, resulting in a more reliable prediction of TKE, which is important for coupling to the wind farm parameterization. The scheme was chosen in part for this property. The MYNN 2.5-level scheme is used for the simulations presented here, in which TKE is a prognostic variable, while all other higher-order quantities are determined diagnostically. All other higher-order turbulent fluxes are expressed in the form of gradient diffusion.

The TKE per unit mass, expressed as $q^2/2$ in the MYNN model, is predicted by the following equation for a dry atmosphere:

$$\frac{\partial q^2}{\partial t} = -\frac{\partial}{\partial z}\langle w'(u'^2 + v'^2 + w'^2 + 2p/\rho_0)\rangle - 2\left(\langle u'w'\rangle\frac{\partial \overline{u}}{\partial z} + \langle v'w'\rangle\frac{\partial \overline{v}}{\partial z}\right) + 2\frac{g}{\overline{\theta}_0}\langle w'\theta'\rangle - 2\varepsilon, \tag{13}$$

where (u', v', w') are the turbulent velocity components, $(\overline{u}, \overline{v}, \overline{w})$ denote the mean components, and the angled brackets denote an ensemble average. Here θ' is the turbulent component of potential temperature and $\overline{\theta}$ is the mean component, p is the pressure, ρ is the air density, g is the gravitational acceleration, and ϵ is the dissipation rate of $q^2/2$, given by

$$\varepsilon = \frac{q^3}{B_1 L}, \tag{14}$$

where B_1 is a closure constant and L is the mixing length.

Horizontal advection of TKE by the model dynamics is employed for the simulations presented here. At higher resolutions, it becomes more important to advect TKE where the TKE is able to persist to downstream grid cells before being dissipated.

The vertical transport and pressure distribution term [the first term on the rhs of Eq. (13)] is expressed in terms of gradient diffusion by

$$-\langle w'(u'^2 + v'^2 + w'^2 + 2p/\rho_0)\rangle = LqS_q\frac{\partial q^2}{\partial z}, \quad (15)$$

where S_q is the stability function for q.

The second and third terms in Eq. (13), the shear and buoyancy terms, respectively, contain second-order turbulent fluxes such as $\langle u'w'\rangle$, which are expressed in terms of gradient diffusion by

$$\langle u'w'\rangle = -LqS_M\frac{\partial \overline{u}}{\partial z}, \quad (16)$$

$$\langle v'w'\rangle = -LqS_M\frac{\partial \overline{v}}{\partial z}, \quad (17)$$

$$\langle w'\theta'\rangle = -LqS_H\frac{\partial \overline{\theta}}{\partial z}, \quad (18)$$

where S_M and S_H are stability functions for momentum and heat, respectively. The eddy diffusivity, K_M, is given by

$$K_M = LqS_M. \quad (19)$$

The wind farm parameterization interacts with the PBL scheme by adding a TKE source (increasing q) and a momentum sink (changing $\partial\overline{u}/\partial z$ and $\partial\overline{v}/\partial z$); therefore, altering the turbulent fluxes [through Eqs. (16)–(18)]. This will be shown to produce a perturbation both within the wind farm and downstream, which the PBL scheme attempts to mix away.

c. Initial conditions

Initial conditions are provided from a prior two-dimensional (2D) run without a wind farm, in which the neutrally stratified boundary layer reaches a steady state. This prior spinup substantially reduces the computational time needed to reach a steady state with the full 3D domain. The 2D grid uses the same configuration as the full domain; however, the lateral boundaries are periodic and there are 25 grid points in the horizontal, with a 1-km resolution and a 3-s time step. The 2D run is initialized with a horizontally uniform potential temperature and geostrophic wind field. The zonal component of the geostrophic wind is 10 m s^{-1} at all levels, and the meridional component is set to zero. The skin surface temperature is set to 285 K, and the vertical potential temperature profile is defined with a neutral layer of the same temperature as the surface, capped with an inversion and stable lapse rate of 3 K km^{-1} aloft. The model is integrated for 360 h, at which time the wind and potential temperature profile within the boundary layer have reached a steady state. The horizontally averaged potential temperature and zonal and meridional components of the wind at each model level from the 2D run provide the initial conditions for the 3D domain. The geostrophic wind forcing used in the 3D domain is the same as in the 2D run.

d. Wind farm configuration

A wind farm of size 10 km × 10 km is placed at the center of the fine grid, with one wind turbine per grid cell, corresponding to a typical turbine spacing of 8 rotor diameters. The turbines modeled are based on the thrust and power coefficients of the REpower 5M turbine, with a nominal power output of 5 MW, a hub height of 100 m, and a blade diameter of 126 m. The cut-in and cut-out wind speeds, below and above which the turbines do not operate, are 3.5 and 30 m s^{-1}, respectively. The proprietary thrust and power coefficients as a function of wind speed were measured by the turbine manufacturer. For the simulations presented here, the wind speed is in the region where the turbine thrust and power coefficients are close to optimal, and vary little with wind speed. A function was fitted to the thrust and power coefficient curves, and incorporated into the model to define the coefficients for a given wind speed. The model is integrated for 30 h, ensuring a steady-state solution.

4. Results

a. Control simulation

This section demonstrates how the boundary layer responds to a large offshore wind farm. A control simulation was performed with a wind farm covering 10 km × 10 km, with the configuration described in section 3c, and is denoted CTRL. A second simulation was performed, in which no wind farm was present, denoted as NF. The impact of the wind farm is assessed by taking the difference between the two simulations. All the results presented are averaged over the last 6 h of the simulations.

The wind farm impacts the mean boundary layer flow as well as the turbulence. The wind speed deficit within

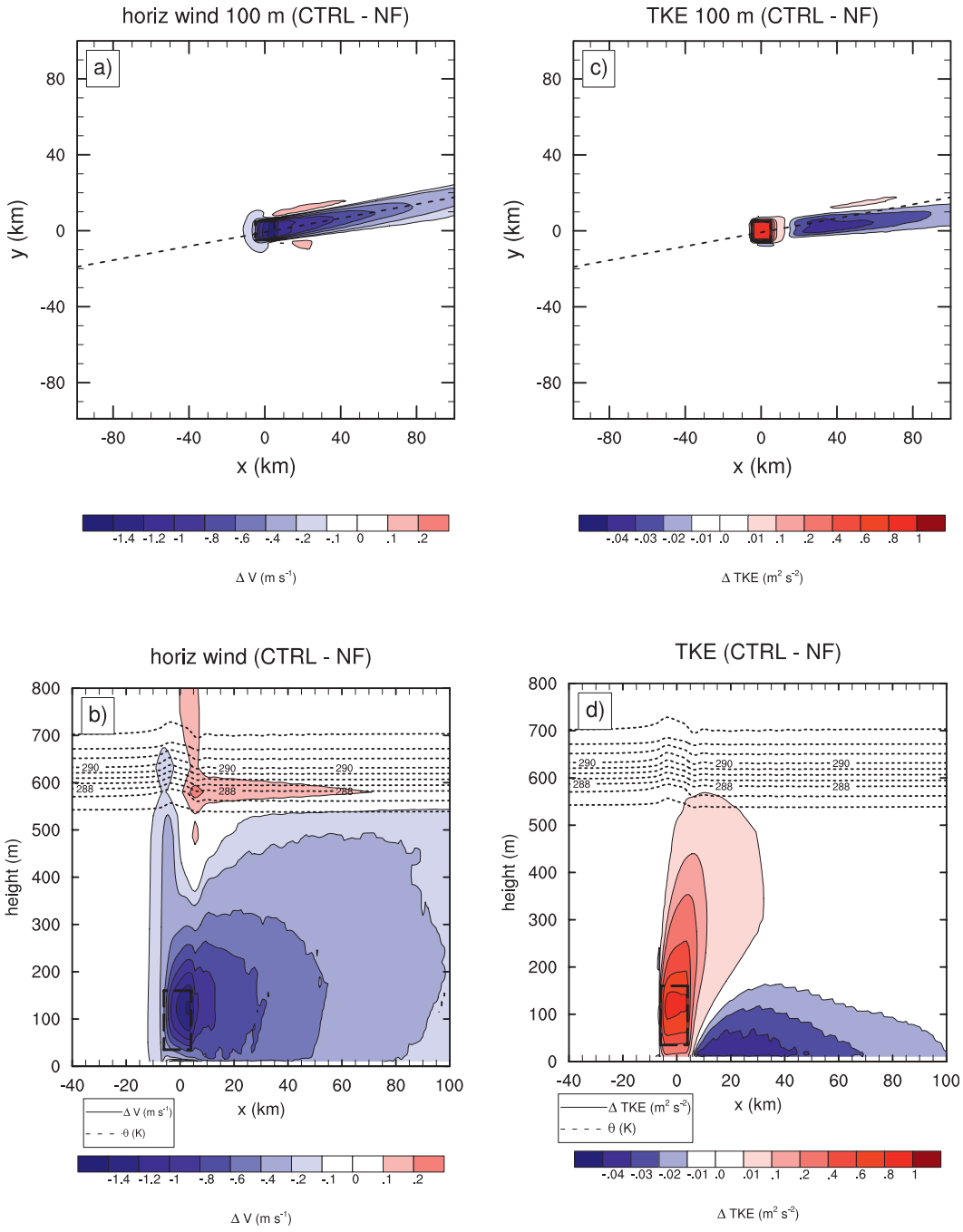

FIG. 2. Horizontal cross sections at hub height (100 m) of (a) horizontal wind speed difference between the control (CTRL) and no–wind farm (NF) simulations; (c) TKE difference. Short-dashed lines indicate the direction of the west-southwesterly wind. Vertical cross sections of the mean difference over the wind farm and wake region of (b) horizontal wind speed and (d) TKE. Short-dashed lines indicate potential temperature and the inversion at the top of the boundary layer; thick long-dashed lines indicate the rotor area.

the farm increases with distance from the upstream edge, as more turbines reduce momentum, and reaches a maximum of 1.5 m s^{-1}, which is a reduction of 16% at the hub-height level (Fig. 2a). Behind the farm, the wind speed deficit extends in a long wake, with an *e*-folding distance of 60 km. A 1 m s^{-1} (11%) deficit reaches 11 km from the downstream edge of the farm. Ekman turning in the boundary layer causes the wake to turn

to the left of the geostrophic wind. Ahead of the farm, the wind is decelerated and a small deficit of 0.1 m s^{-1} or 1% extends 15 km from the upstream edge. On the flanks of the wake a small acceleration (maximum 0.1 m s^{-1}, 1%) is seen. The wind speed deficit in the wake compares well with observations from Christiansen and Hasager (2005), where a 8%–9% reduction at a height of 10 m was seen immediately downstream of the Horns Rev and Nysted offshore wind farms in Denmark. Here, a 10% reduction in the wind at 10 m is observed. The Horns Rev and Nysted wind farms are somewhat smaller than that modeled here—the largest, Horns Rev, covers 19 km^2 and consists of 80 turbines of 2-MW nominal power, with hub heights and blade diameters of 70 and 80 m, respectively.

The wind speed deficit is spread throughout the BL above and downstream from the farm (Fig. 2b). A 1 m s^{-1} deficit extends to a height of approximately 200 m. Near the surface within the wind farm, the wind is accelerated with respect to the NF case by up to 0.7 m s^{-1}, an increase of 11%. This shallow accelerated region extends downstream and a deficit is not observed until 4 km beyond the downstream edge of the farm (not shown). Above the farm, the height of the BL increases by up to 17 m, and in the wake drops by up to 12 m, which is reflected in the potential temperature profile.

The generation of TKE within the wind farm is largely restricted to the farm area, and quickly decays downstream with an *e*-folding distance of 1.5 km (Fig. 2c), despite the advection of TKE. A maximum increase of TKE of 0.9 m^2 s^{-2} is seen within the farm, an increase close to a factor of 7 relative to the NF case. Unlike the wind speed deficit, the difference in TKE is largely uniform across the wind farm. An increase in TKE of 0.4 m^2 s^{-2}, a factor of nearly 3, extends 1 km downstream from the farm at hub-height level. Beyond 10 km downstream, a reduction of maximum 0.04 m^2 s^{-2} (27%) is observed.

The reduction of TKE near the surface downstream (Fig. 2d) results from the wind speed deficit, and the corresponding reduction in the wind shear at lower levels in the wake, which leads to a reduction in shear production of TKE (shown in section 4b). The reduction of TKE in the wake extends along the full length of the wake simulated here, but does not reach a height greater than the top of the turbines. Near the surface within the farm there is an increase in TKE, of 0.1 m^2 s^{-2}, an increase by a factor of 2 relative to the NF case. The increase in TKE persists up to 6 km downstream near the surface. These results are consistent with Chamorro and Porté-Agel (2009), who report an increase of turbulence in the very far wake region of wind-tunnel experiments with a single turbine, 15 rotor diameters downstream (corresponding to 1.9 km here). However, they found a decrease in turbulence in the lower region of the wake due to the reduction of wind shear, also reported by Lu and Porté-Agel (2011), and observed here.

In the vertical, the increase in TKE spreads to the top of the BL above the wind farm (Fig. 2d), with a 0.5 m^2 s^{-2} increase extending to a height of nearly 280 m, an increase by a factor of 5 relative to the NF case. At 500 m (near the top of the BL), the TKE increases by a factor of 2. At the mid- to upper levels of the BL, the increase in TKE extends farther downstream than at lower levels; however, near the surface, the TKE decreases relative to the NF case.

The change in wind speed and TKE seen around the wind farm could be considered a manifestation of an internal BL that has formed in response to the change in roughness presented by the farm, except that it has penetrated throughout the depth of the BL. The adjustment of the impinging flow consists of an upstream deceleration and, by continuity, vertical motion that penetrates throughout the depth of the BL into the stable layer overlying the BL (Fig. 2b). The perturbation within the stable portion of the atmosphere is in the form of a gravity wave.

b. TKE budget

The TKE budget was computed using Eq. (13) to highlight the mechanisms that impact the net TKE in different regions. The main source of TKE is explicitly added by the wind turbine parameterization within the rotor area. Outside of the rotor area, the largest source of TKE is vertical transport (Fig. 3a) and shear production (Fig. 3b). The TKE generated within the rotor area is transported away in the vertical, leading to a reduction in the TKE above hub height to a height of approximately 200 m (40 m above the turbine blades; Fig. 3a). The TKE is reduced most by vertical transport at the top of the rotor area. Below hub height to the surface, the TKE is increased by vertical transport, with a maximum at the bottom of the rotor area. From approximately 200 m to the upper levels of the BL, the TKE increases by vertical transport.

The momentum deficit within the rotor area generates shear production of TKE at the top of the rotor area and above to a height of around 400 m (240 m above the turbine blades; Fig. 3b). Below hub height, within the farm, and near the surface in the wake, the wind shear is reduced, which leads to a reduced shear production of TKE in these regions. The production of TKE by buoyancy is negligible compared with the other terms owing to the neutral BL (not shown).

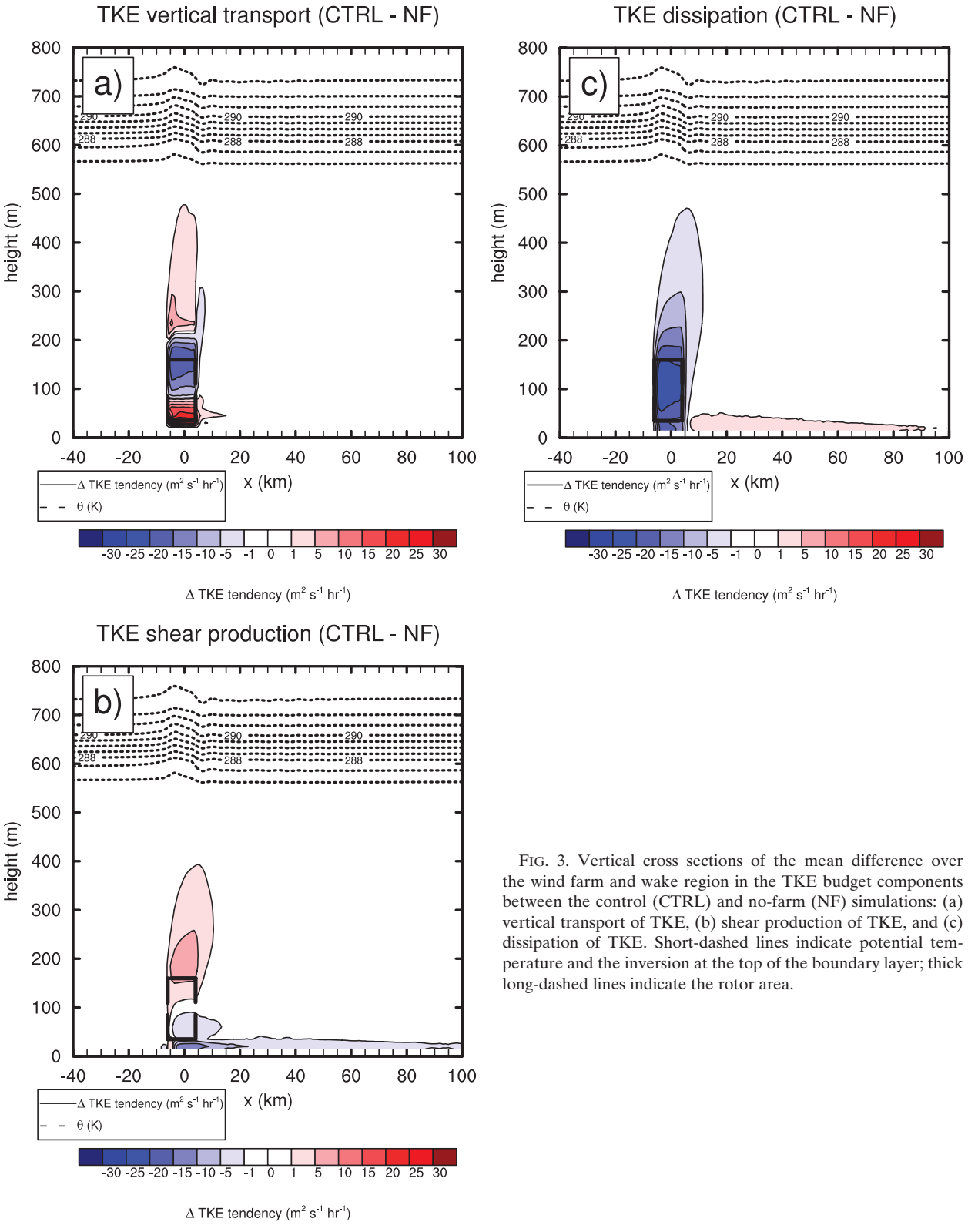

FIG. 3. Vertical cross sections of the mean difference over the wind farm and wake region in the TKE budget components between the control (CTRL) and no-farm (NF) simulations: (a) vertical transport of TKE, (b) shear production of TKE, and (c) dissipation of TKE. Short-dashed lines indicate potential temperature and the inversion at the top of the boundary layer; thick long-dashed lines indicate the rotor area.

The dissipation of TKE is high within the rotor area (Fig. 3c) due to the dependency on q^3 in the dissipation term [Eq. (14)], where TKE = $q^2/2$. There is also greater dissipation of TKE (relative to NF) near the surface below the turbines, and above to around 500 m (340 m above the turbines), corresponding to the areas where TKE is increased. Downstream in the wake near the surface the dissipation (relative to NF) is reduced owing to the reduction of wind shear and associated TKE production.

More advection of TKE into the wake is seen at mid- to upper levels of the BL, where the dissipation is less and the wind speed is greater. The mixing length at this height is close to a factor of 2 greater than at hub height, which in turn reduces the dissipation through Eq. (14).

c. *Analysis of the parameterization components*

To investigate how the separate components of the parameterization behave, and their impact on the BL flow, two additional experiments were performed: one with only the momentum sink component of the parameterization active (denoted SINK), and the other with only the TKE source active (denoted TKE). Figure 4a shows the vertical profile of the mean difference in horizontal wind over the wind farm area (F) and 10–20 km downstream (D). The mean is computed over a 10 km $\times$ 10 km square in each case. Within the rotor area, the velocity deficit is predominantly from the momentum sink, and reaches a maximum of -1.2 m s^{-1} (in CTRL). The momentum sink causes deceleration throughout the depth of the BL. The TKE source accelerates the wind within the rotor area and below in the CTRL case (relative to SINK), by mixing air with higher momentum from upper levels down. The TKE source reduces the maximum wind deficit in the CTRL case by 0.4 m s^{-1} (relative to SINK) within the rotor area, a reduction of 25%, and increases the near-surface wind by 0.8 m s^{-1}, an increase by a factor of nearly 3. Above the farm, the momentum sink and TKE terms contribute almost equally to the wind speed deficit. The TKE source mixes air with lower momentum within the farm to higher levels. The wind shear over the rotor area is reduced from the NF case, mostly due to the TKE source. Downstream of the wind farm, at 10 km (denoted D in Fig. 4a), the wind speed deficit is reduced to a maximum of 0.8 m s^{-1} in CTRL, a reduction of 33%.

The horizontal wind speed is dominated by the zonal component (Fig. 4b) because the simulations are initialized without a meridional component. However, the Coriolis force gives rise to a meridional component (Fig. 4c), which varies with height owing to differences in friction and turbulence (the Ekman spiral). The Ekman turning is reduced within the rotor area and below, due to the enhanced mixing by the wind farm reducing the meridional component of the wind. The momentum sink is responsible for directly reducing the wind in the rotor area. Conversely, the enhanced mixing mechanism is responsible for the increased meridional wind component above the wind farm, leading to enhanced Ekman turning there.

The TKE source term within the rotor area increases TKE throughout the depth of the BL above and below the farm (Fig. 5a). The momentum sink term induces shear production of TKE (Fig. 3b) at the top of the turbines due to the momentum deficit within the farm, leading to an increase of TKE in this region (Fig. 5a). Below the farm, the wind shear is reduced, causing a reduction of TKE in the SINK case (relative to NF), and in CTRL (relative to TKE).

Figure 6a shows the difference in the horizontal wind averaged in the vertical over the rotor area, and in the horizontal across the farm and wake region. The TKE source accelerates the wind through the wind farm and downstream to 35 km, causing a reduction in the net wind deficit of 0.2 m s^{-1} ($\sim$22%), 10 km downstream in the CTRL case, relative to SINK.

Figure 6b shows the difference in TKE averaged in the vertical over the rotor area, and in the horizontal across the farm and wake region. The increase in TKE is mostly confined to the wind farm area, and is largely uniform across the farm. Downstream in the CTRL and TKE cases, the TKE quickly decays as there is strong dissipation within the farm and less wind shear than in the SINK case. Farther downstream, there is a small reduction of TKE relative to the NF case, as the wind deficit within the wake reduces shear production of TKE.

The TKE generated within the farm significantly increases the momentum eddy diffusivity (K_M; Fig. 5b) within the rotor area and throughout the BL. The turbulent momentum fluxes are, in turn, significantly enhanced (discussed in the next section). In the CTRL case, there is a maximum increase of 12 m^2 s^{-1} in the eddy diffusivity in the rotor area relative to the NF case, an increase by a factor of 4. Up to a height of 450 m, the eddy diffusivity is increased by a factor of 2. In the SINK case (long dashed lines, Fig. 5b), there is a sharp kink in the eddy diffusivity profile at the top of the rotor area. This signature is caused by the enhanced shear (reducing the stability function for momentum, and in turn the eddy diffusivity), in which the PBL scheme is acting to flux momentum back into the deficit induced by the momentum sink.

Calaf et al. (2010) and Lu and Porté-Agel (2011) employed a nondimensional parameter, called the ''wake eddy diffusivity'' to quantify the enhancement of the

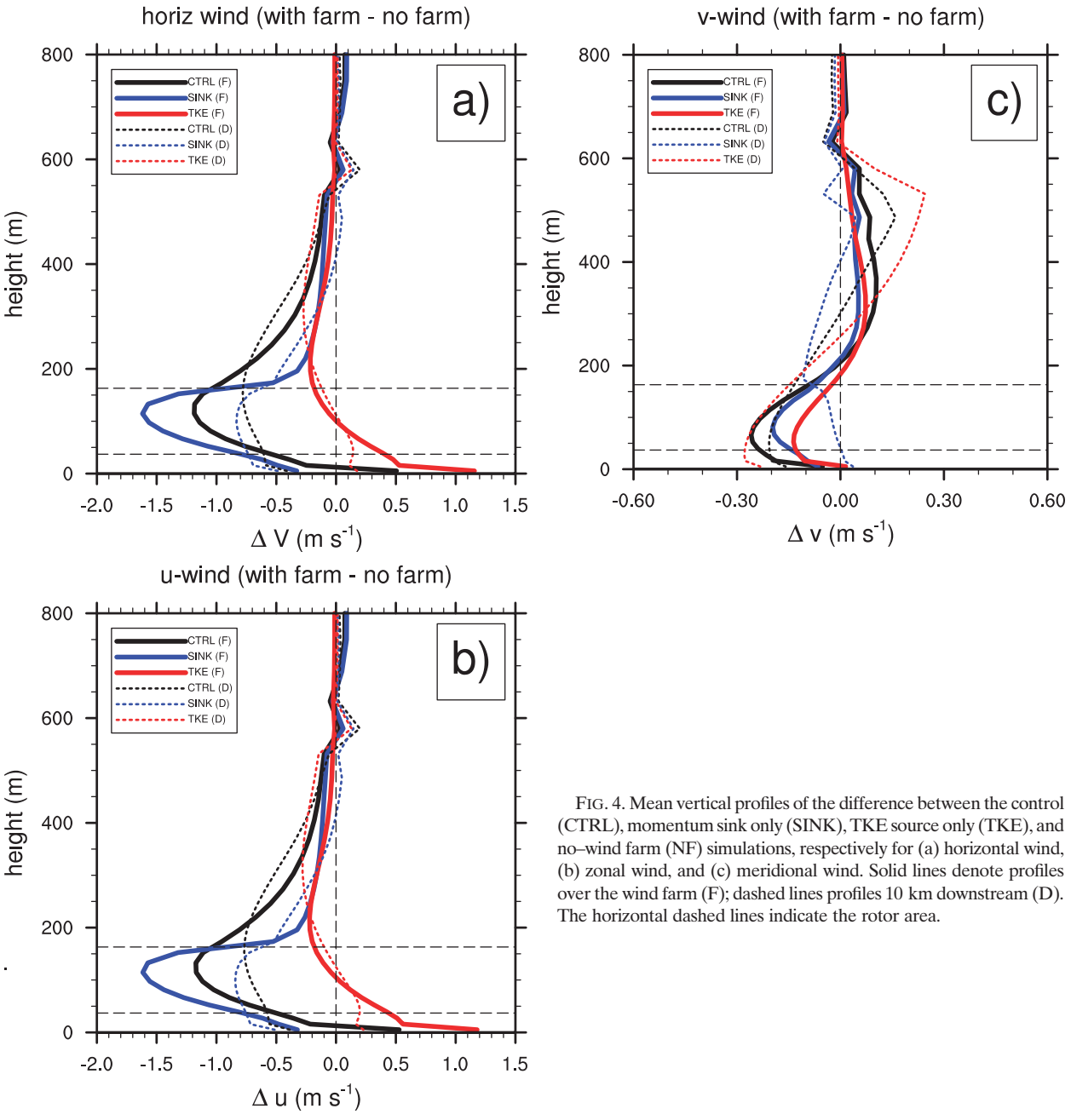

FIG. 4. Mean vertical profiles of the difference between the control (CTRL), momentum sink only (SINK), TKE source only (TKE), and no–wind farm (NF) simulations, respectively for (a) horizontal wind, (b) zonal wind, and (c) meridional wind. Solid lines denote profiles over the wind farm (F); dashed lines profiles 10 km downstream (D). The horizontal dashed lines indicate the rotor area.

eddy diffusivity associated with turbine mixing in their LES of a wind farm, here defined as

$$K_w = (K_{\mathrm{CTRL}} - K_{\mathrm{NF}})/K_{\mathrm{NF}}, \tag{20}$$

where K_{CTRL} and K_{NF} are the mean eddy diffusivities over the rotor area in the CTRL and NF cases, respectively. From their LES, Calaf et al. (2010) introduced a model for the wake eddy diffusivity as a function of turbine characteristics, given by

$$K_w = 28\sqrt{\frac{1}{2}\frac{\pi C_T}{4 s_x s_y}}, \tag{21}$$

where C_T is the turbine thrust coefficient, and s_x and s_y is the turbine spacing in rotor diameters in the zonal and meridional directions, respectively.

Lu and Porté-Agel (2011) calculated the "effective" eddy diffusivity based on the total momentum fluxes

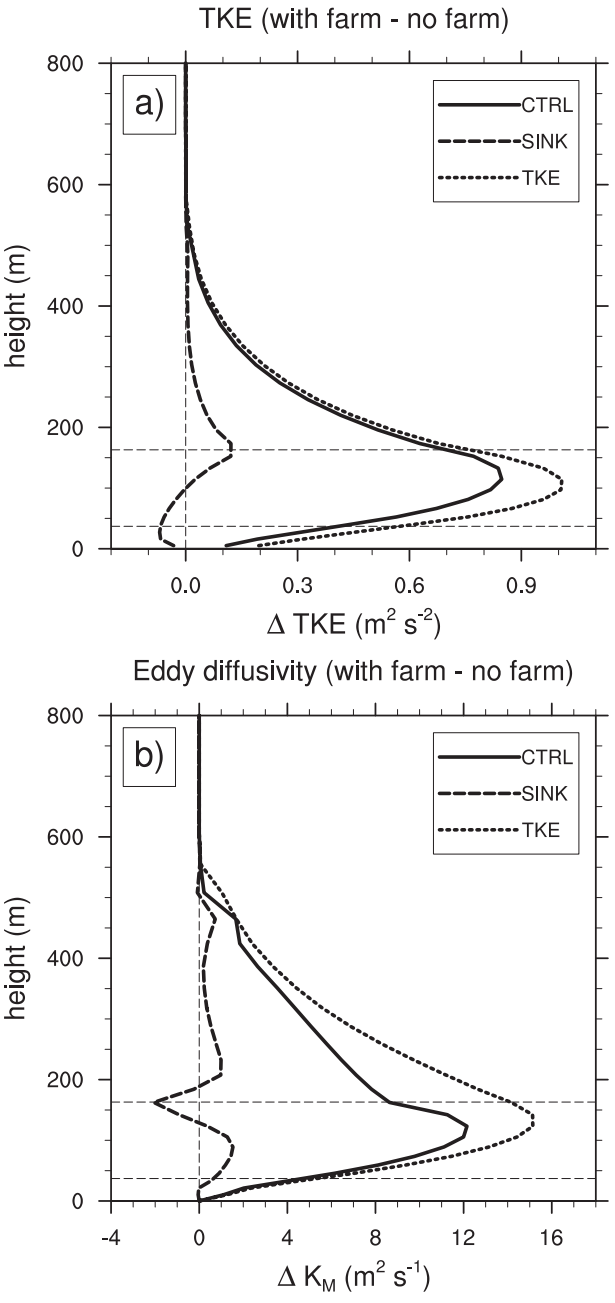

FIG. 5. Mean vertical profiles highlighting the parameterization components. The difference between the control (CTRL), momentum sink only (SINK), TKE source only (TKE), and no–wind farm (NF) simulations, respectively, is shown for (a) TKE and (b) momentum eddy diffusivity. The horizontal dashed lines indicate the rotor area.

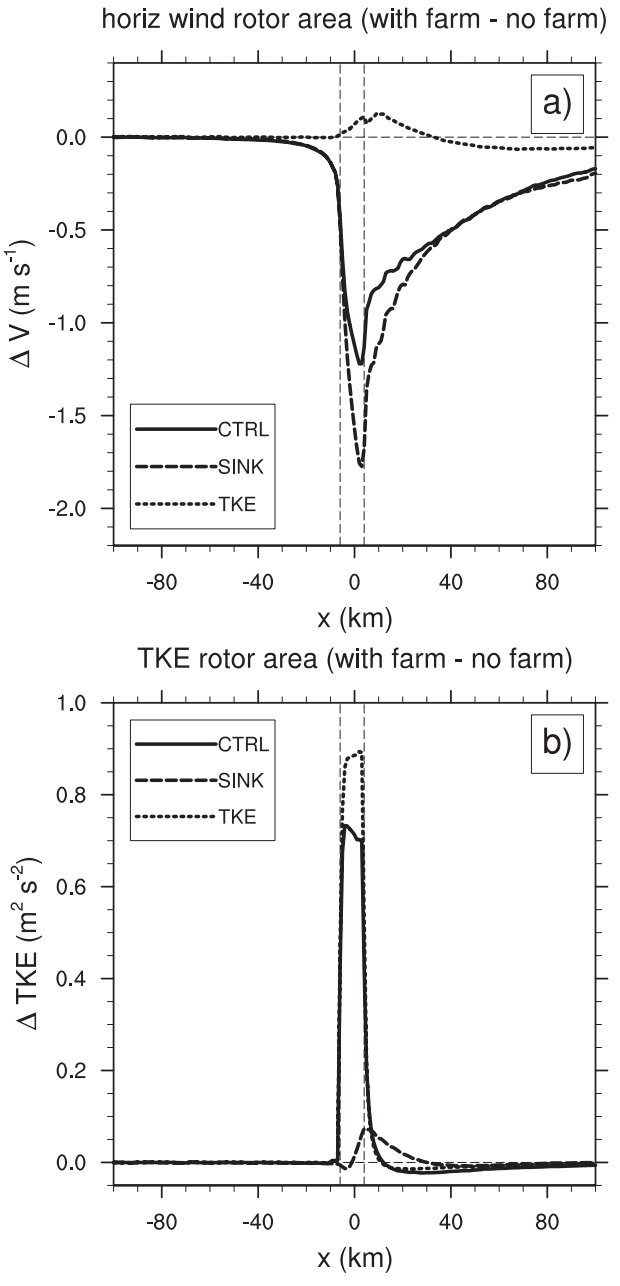

FIG. 6. Horizontal profiles highlighting the parameterization components. The profiles averaged vertically over the rotor area and horizontally over the wind farm and wake region are shown for (a) horizontal wind speed difference and (b) TKE difference. The dashed vertical lines indicate the wind farm area.

and mean wind shear obtained in their LES of a wind farm, and in turn obtained the wake eddy diffusivity.

We find a value of K_w of 3.4, corresponding to an intermediate value using the model from Calaf et al. (2010) [Eq. (21), where C_T is averaged over the rotor area] and the LES measurement from Lu and Porté-Agel (2011), where values of 1.92 and 4.16 are obtained, respectively. The discrepancy in values could be due to the different stratification and depths of the boundary layers simulated—our simulations are of a neutral BL of an intermediate depth to that in Calaf et al. (2010) and Lu and Porté-Agel (2011), where the former simulated

a deeper BL than the latter. Calaf et al. (2010) also simulated a neutrally stratified BL; however, Lu and Porté-Agel (2011) simulated a stably stratified BL. In addition, the averaging operation employed in Lu and Porté-Agel (2011) could give different results depending on the exact order of the operation.

d. Momentum tendencies and turbulent fluxes

The momentum tendencies from the physics parameterizations are shown in this section to highlight how the PBL scheme and the wind farm parameterization work together to create the perturbation around the wind farm. The tendencies arise from the vertical divergence of the turbulent fluxes. The turbulent momentum fluxes were calculated using Eqs. (16) and (17), and the tendencies output from the model.

The downward flux of zonal momentum is enhanced within the wind farm area and above to the top of the BL (shown by the negative region in Fig. 7a), by up to $-0.17\ m^2\ s^{-2}$ at the top of the turbines. This increase corresponds to an increase in the magnitude of the flux by more than a factor of 5 relative to NF. Greater downward flux of zonal momentum also is seen at mid- to upper levels of the BL downwind of the farm, corresponding to regions where the wind shear and TKE are enhanced relative to NF. Behind the wind farm in lower regions of the wake, the downward flux is reduced owing to a reduction of TKE and wind shear in this region (indicated by the positive region in Fig. 7a). Near the surface within the front side of the farm, the downward momentum flux is enhanced by a maximum of nearly a factor of 2. However, near the surface in the rear end of the farm and wake, the flux is reduced by up to a factor of 1.3. Figure 7b shows the zonal momentum tendency difference between the CTRL and NF cases. A strong deceleration results within and above the wind farm region. In contrast, immediately behind the wind farm, the zonal wind is accelerated.

The momentum sink enhances the downward zonal momentum flux above hub height, and decreases it below (Fig. 7c), which is responsible for most of the zonal wind acceleration behind the wind farm (Fig. 7d). The TKE source is responsible for the greater vertical extent of enhanced momentum flux (Fig. 7e) and zonal wind deceleration (Fig. 7f) above the farm. These results compare well with LES performed by Lu and Porté-Agel (2011), who found the momentum flux was greatest at the top of the turbines due to the enhanced mixing of momentum by the turbines in that region. They also found the momentum flux was enhanced above hub height and decreased below.

The upward flux of meridional momentum is enhanced above the wind farm by up to $0.02\ m^2\ s^{-2}$ at a height of 300 m in the CTRL case, an increase by close to a factor of 2 relative to NF (Fig. 8a). The region of enhanced flux extends to the top of the BL and is caused primarily by the TKE source (Fig. 8e). The upward flux of momentum leads to acceleration in a narrow region above the farm (Figs. 8b,f). Therefore, the enhanced mixing, primarily caused by the TKE source, acts to increase Ekman turning above the farm and decrease Ekman turning below.

e. Sensitivity to the magnitude of the TKE source

To explore the sensitivity to the magnitude of the TKE source in the parameterization, two simulations changing the TKE were carried out. One experiment was conducted with the source of TKE doubled, denoted DTKE, and the other with the source of TKE halved, denoted HTKE. Figure 9a shows the mean vertical profile of the horizontal wind speed difference over the wind farm between the DTKE, HTKE, CTRL and NF cases. The DTKE case causes a reduction in the wind speed deficit within the farm with respect to the CTRL case, but increases the deficit above the wind farm by enhanced vertical mixing of momentum. In contrast, the HTKE case shows a greater deficit within the farm and smaller deficit above as the vertical mixing is reduced.

Within the rotor area, the doubling or halving of the TKE source leads to a maximum uncertainty of $\pm 0.1\ m\ s^{-1}$ in the horizontal wind, an uncertainty of less than 10% of the response to the wind farm in the CTRL case. At the surface, this uncertainty increases to $\pm 0.2\ m\ s^{-1}$ (40% of the response to the wind farm in the CTRL case), with the DTKE case giving a greater increase in the wind speed.

Figure 9b shows the difference in the horizontal wind speed averaged in the vertical over the rotor area, and in the horizontal across the farm and wake region. The maximum uncertainty in the wake increases to $\pm 0.15\ m\ s^{-1}$ (18% of the response to the wind farm in CTRL), approximately 5 km downstream. Some uncertainty extends along the wake up to 35 km downstream. In general, it appears the uncertainty in parameterizing the magnitude of the TKE source term results in less than a $\pm 20\%$ uncertainty in the total perturbation induced by the wind farm parameterization.

f. Sensitivity to vertical resolution

The sensitivity of the results to vertical resolution was tested by conducting an experiment, in which the number of vertical model levels was halved, denoted HV (Fig. 1). The lowest level was kept the same to reduce the sensitivity the surface momentum flux may have on the depth of the lowest model layer. Figure 10a

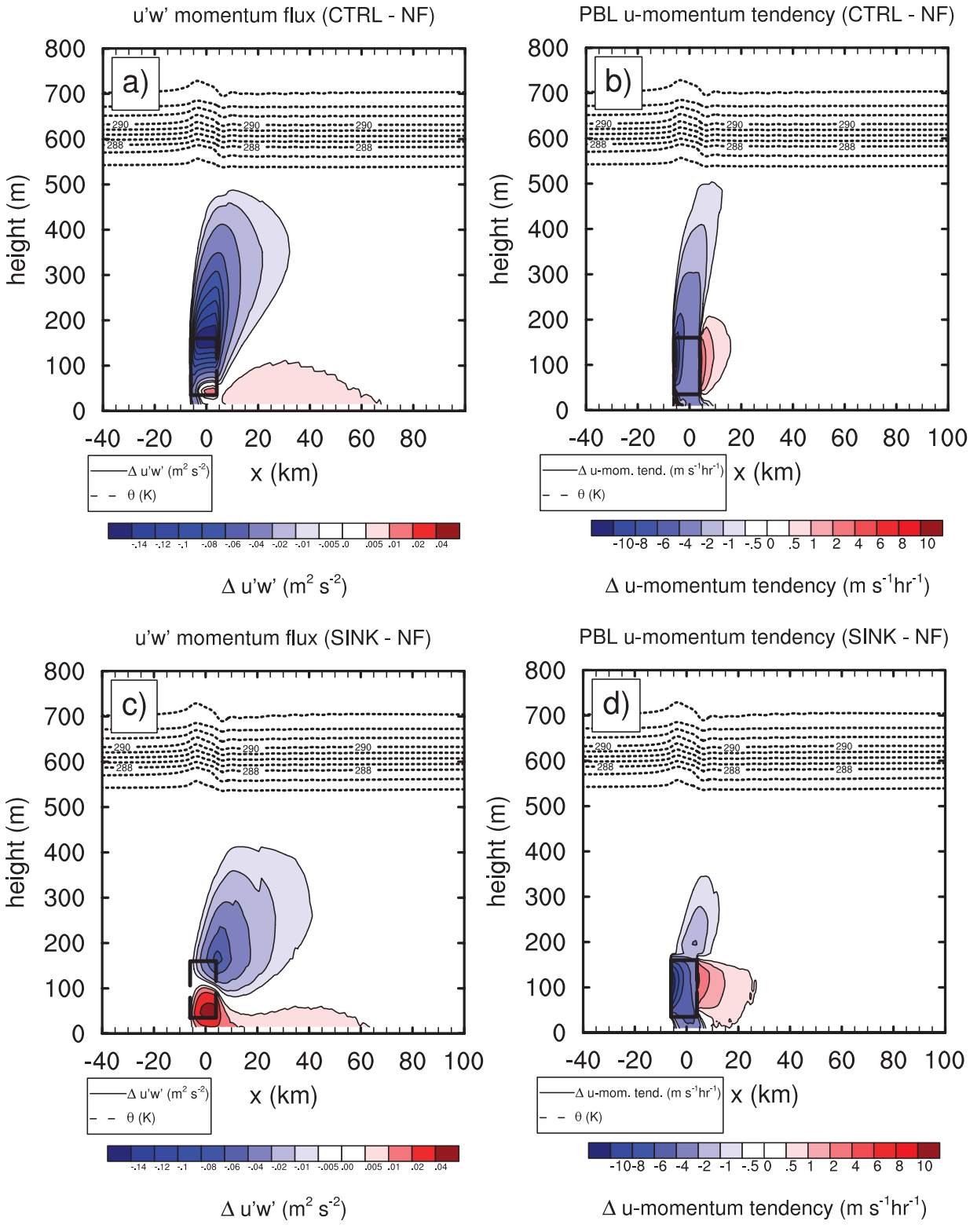

FIG. 7. Vertical cross sections over the wind farm and wake region of the mean (left) zonal momentum flux and (right) zonal momentum tendency for (a),(b) difference between control (CTRL) and no–wind farm (NF) simulations; (c),(d) difference between momentum sink only (SINK) and NF; (e),(f) difference between TKE source only (TKE) and NF. Dashed lines are as in Fig. 3.

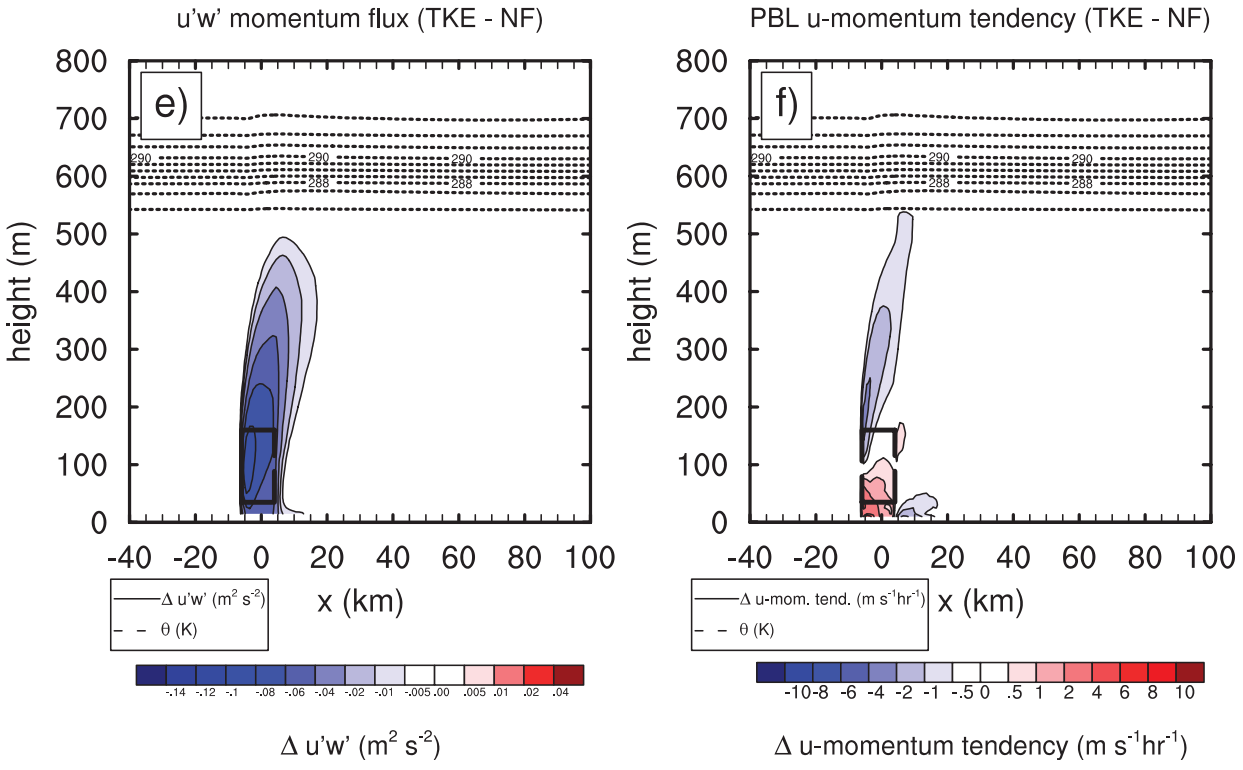

FIG. 7. (*Continued*)

highlights the sensitivity of the PBL scheme (without the wind farm) to halving the vertical resolution. The difference in horizontal wind between the half resolution and standard resolution cases, both without a wind farm, is shown. Overall, there is little sensitivity. The maximum difference in wind speed is 0.2 m s^{-1}, located within the inversion, with the lower-resolution simulation exhibiting stronger winds. The other region of greatest difference ($\pm$0.1 m s^{-1}) is close to the surface, below 50 m. The lower resolution weakens the wind shear near the surface, resulting in stronger surface layer winds.

Figure 10b shows the sensitivity of the wind to vertical resolution in the presence of the wind farm. Again, there is little sensitivity. Below the rotor area, and up to 15 km downstream, the lower resolution leads to a reduction in the wind speed of up to 0.1 m s^{-1}. This corresponds to an uncertainty of 20% of the response in CTRL.

Further experiments were carried out in which the vertical levels were the same as the CTRL experiment, apart from inside the rotor area where the number of levels was reduced. When the number of levels intersecting the rotor area was greater than one, little sensitivity was seen compared to CTRL (not shown). Even when the rotor area was contained within only one model level, the mean wind speed within the wind farm was approximately the same as CTRL. However, downstream the uncertainty in the horizontal wind speed increased to a maximum of 33% of the response to the wind farm in the CTRL case. An uncertainty persisted for the whole length of the wake in the domain.

In summary, the sensitivity to vertical resolution appears to be less than 10% of the response to the wind farm within the rotor area and downstream; thus, the wind farm parameterization should yield reasonable results for applications with limited resources.

g. Sensitivity to horizontal resolution

To investigate the sensitivity of the results to horizontal resolution, experiments were performed with the horizontal grid size doubled to 2 km, both with and without the wind farm (denoted HH and HHNF, respectively). The density of wind turbines was kept constant by increasing the number of turbines per grid cell to 4. Without the wind farm, the difference in wind speed between the 1- and 2-km simulations was found to be negligible. With the addition of the wind farm, a maximum reduction in the wind of 0.1 m s^{-1} was found in the rotor area in the 2-km case (Fig. 11a). The simulations were compared by area averaging of the results on the fine grid to the coarse grid.

Figure 11b shows the difference in TKE between the 1- and 2-km simulations. An increase of maximum

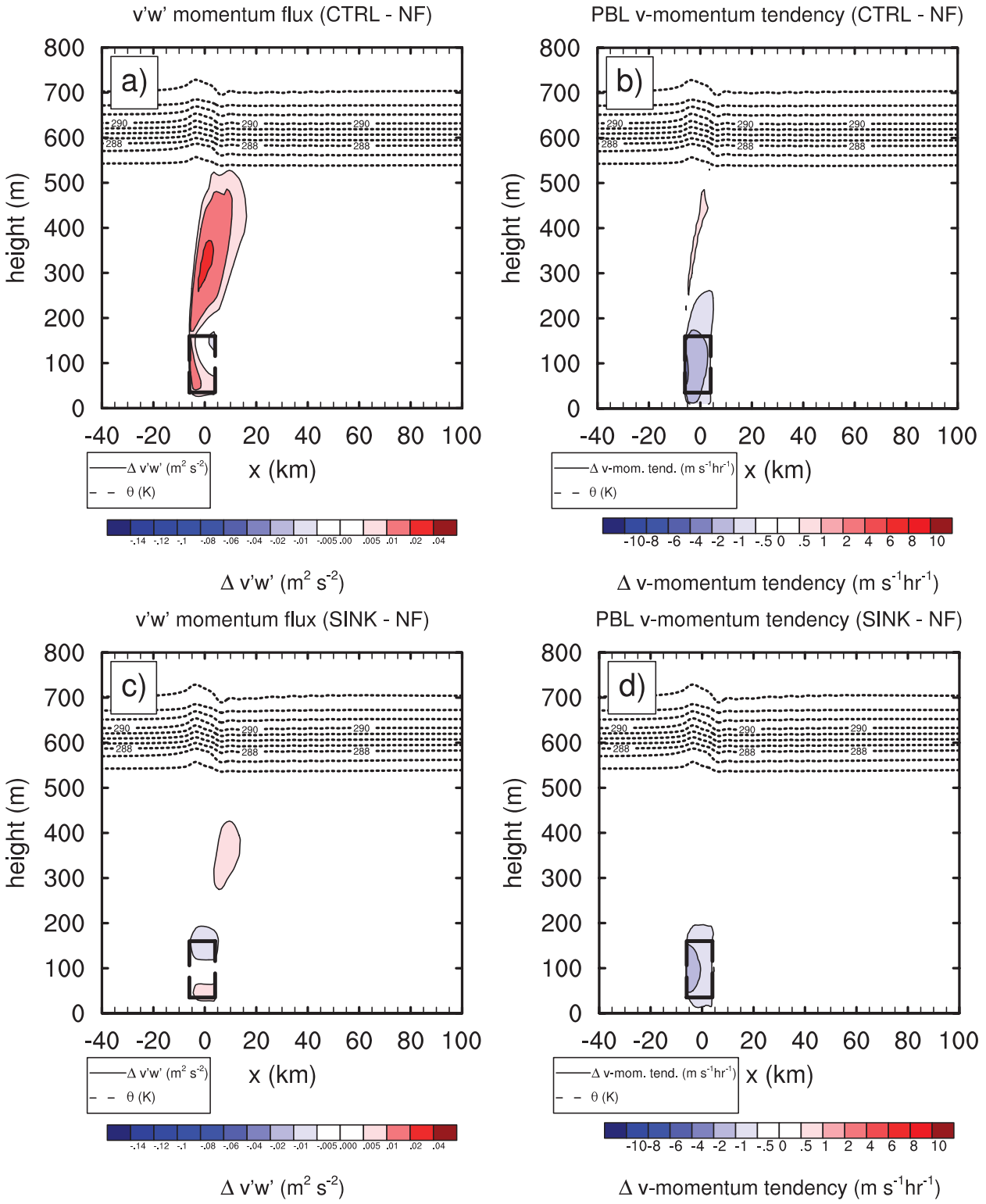

FIG. 8. As in Fig. 7, but for meridional momentum flux and tendency.

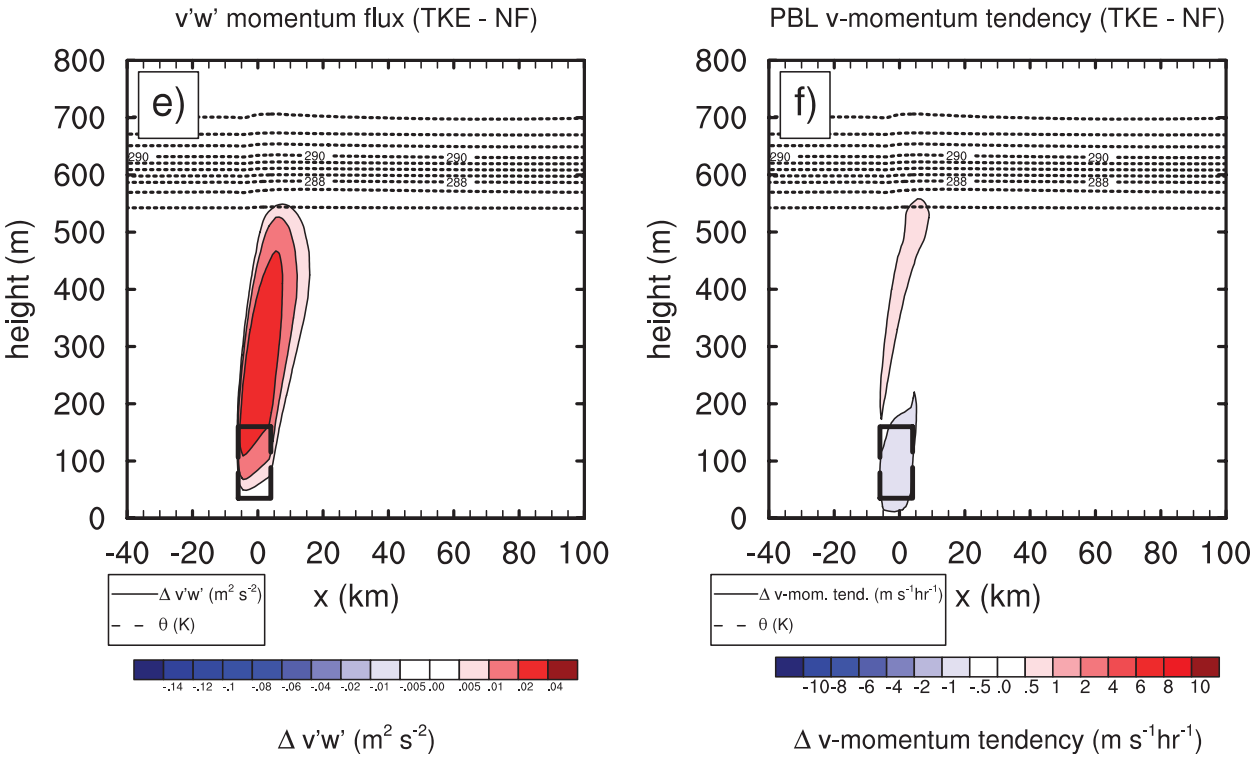

FIG. 8. (*Continued*)

0.1 m^2 s^{-2} is seen along the upstream edge of the farm, with a slightly smaller decrease along the downstream edge. This difference is thought to result from the differences in TKE advection.

h. Power output

The power output was calculated for each grid cell containing wind turbines using the power coefficient as the fraction of energy extracted from the atmosphere that is converted into useful energy by the turbines [Eq. (11)]. Figure 12 shows the fractional power output (the power for each turbine divided by the maximum power output of a turbine in the wind farm) for each turbine in the wind farm. The greatest power output is observed in the turbines along the upstream edges of the farm (in this case the west and south boundaries of the farm, owing to the mean west-southwesterly flow at hub height), as expected. Behind the upstream edges, the power output decreases to a minimum of 65% of the most productive turbine. The power loss compares well with observations from the Horns Rev and Nysted wind farms (Barthelmie et al. 2007, 2010). A nonsymmetrical pattern across the wind farm is observed, owing to the orientation of the mean wind vector with respect to the farm. The turbines producing the most power are located at the corner of the wind farm most exposed to the wind (i.e., the southwest corner), with the least productive turbines at the downstream edge of the wind farm. The KE recovers more slowly behind turbines that have extracted more energy, and hence the least productive turbines are found at the farthest edge of the wind farm behind the most productive turbines following the direction of the mean wind.

5. Discussion and conclusions

A new wind farm parameterization has been developed for the mesoscale numerical weather prediction model WRF (released in version 3.3), which provides a tool to improve understanding of the interaction between wind farms and the atmospheric boundary layer. Wind turbines are represented as a momentum sink and a source of turbulence (TKE) at model levels containing turbine blades. The wind farm parameterization developed here improves upon previous mesoscale simulations by representing turbine drag using the thrust coefficient data from a modern commercial turbine. The thrust coefficient is the total fraction of kinetic energy extracted from the atmosphere due to wind turbines, and is a function of wind speed. Other parameterizations have based this fraction on the power coefficient (the

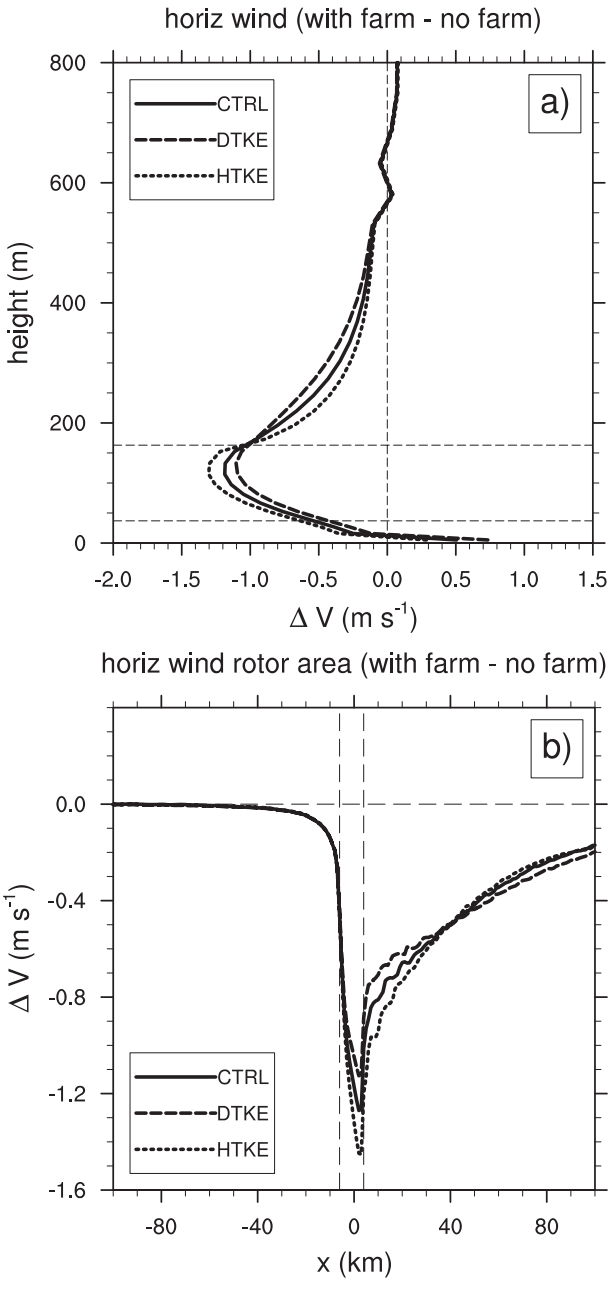

FIG. 9. Profiles highlighting the sensitivity of the horizontal wind speed to the magnitude of the source of TKE. The difference between the control (CTRL), double TKE source (DTKE), half TKE source (HTKE) and no–wind farm simulations, respectively, are shown for (a) the mean vertical profile over the wind farm, with the rotor area indicated by the horizontal dashed lines; and (b) the horizontal profile averaged vertically over the rotor area and horizontally over the wind farm and wake region, with the wind farm area indicated by the vertical dashed lines.

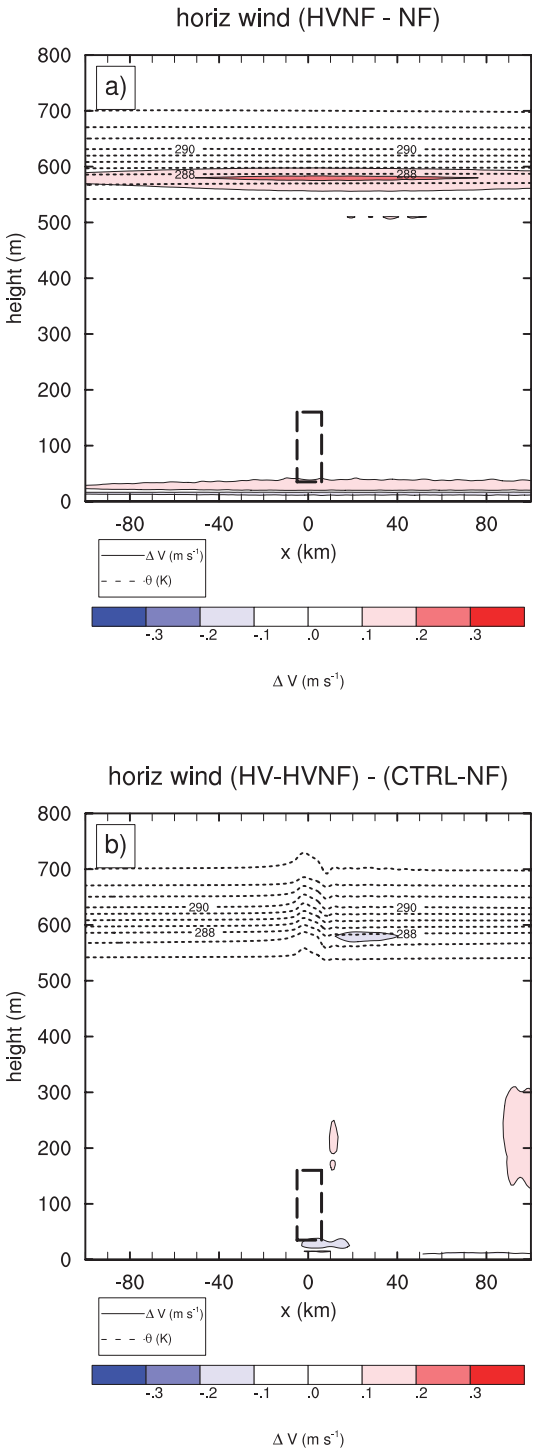

FIG. 10. Vertical cross sections highlighting the sensitivity of the mean horizontal wind speed over the wind farm and wake region to vertical resolution. (a) The difference in horizontal wind speed between the half vertical resolution (HVNF) and control resolution (NF) simulations, both without a wind farm. (b) The difference in horizontal wind speed between the half vertical resolution simulation with the wind farm (HV) and the control simulation (CTRL). Dashed lines are as in Fig. 3.

fraction of energy extracted that is converted into useful electrical energy), either neglecting turbine losses (Baidya Roy 2011) or estimating the loss fraction and adding it to the power coefficient (Blahak et al. 2010). In

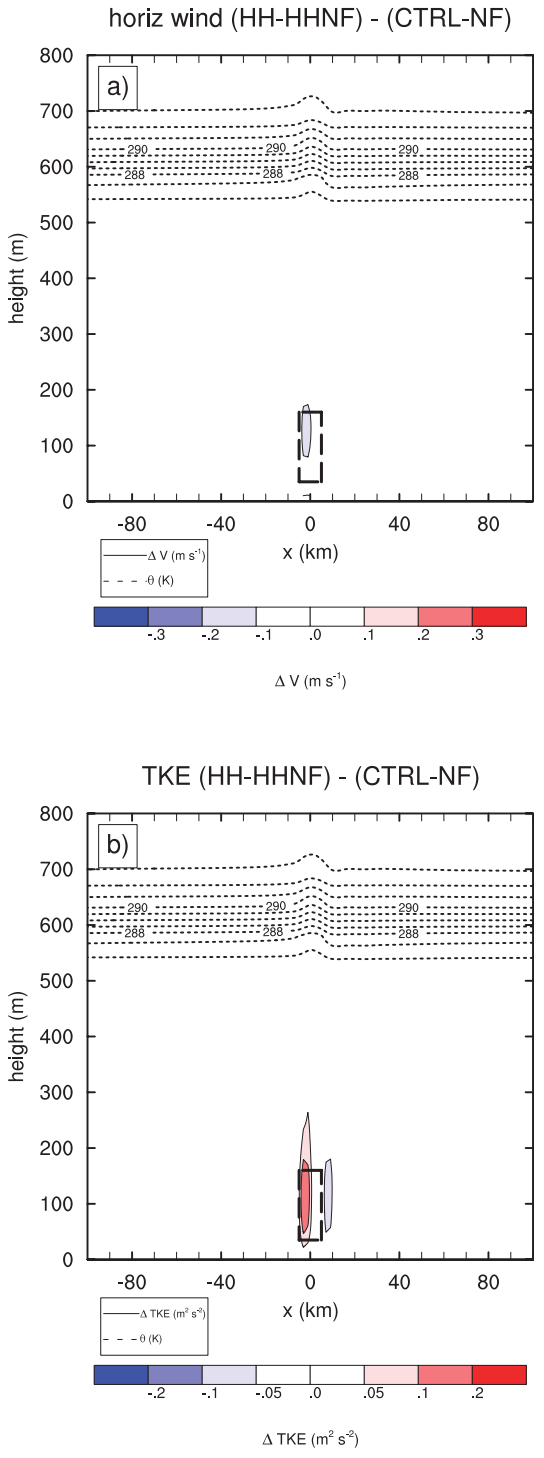

FIG. 11. Vertical cross sections highlighting the sensitivity of the mean horizontal wind speed and TKE over the wind farm and wake region to the horizontal resolution. (a) The difference in horizontal wind speed between the half horizontal resolution with the wind farm (HH) and control resolution (CTRL) simulations. (b) The difference in TKE between the half horizontal resolution simulation with the wind farm (HH) and the control simulation (CTRL). Dashed lines are as in Fig. 3.

the former, the drag on the atmosphere will be underestimated (by up to a factor of nearly 6 in the turbines modeled here), and in the latter there is some uncertainty regarding the loss factor chosen.

Another improvement is in the representation of TKE generated by the turbines. Previous studies have set the fraction of energy extracted by the turbines, which is converted into TKE, to a constant. In practice, it should be a function of wind speed. Some fraction (the TKE coefficient) of the kinetic energy extracted by the turbines, which is not converted into electrical energy, should produce TKE. Here, we assumed mechanical and electrical losses in the turbines are minimal, and that all of the energy remaining after conversion into electricity generates TKE. Thus, the TKE source is overestimated; although, given that modern turbines have been designed to keep losses to a minimum, this overestimate should be rather small. If data regarding the losses in the turbines under study are known, this can be used to more accurately define the TKE coefficient.

Idealized simulations of a large offshore wind farm were carried out to demonstrate the parameterization and explore the interaction between the wind farm and the BL. For an offshore wind farm covering 10 km $\times$ 10 km with 100 turbines of nominal power 5 MW, significant impacts on wind speed, turbulent kinetic energy, and momentum fluxes were found. The wind speed deficit within the farm reached a maximum of 1.5 m s^{-1}, a reduction of 16% at the hub-height level. The wind speed deficit extended throughout the depth of the neutral boundary layer, above and downstream from the farm, with a long wake of 60-km *e*-folding distance. Near the surface within the wind farm, the wind was accelerated by up to 11%.

A maximum increase of TKE of 0.9 m^2 s^{-2} was seen within the farm, an increase close to a factor of 7 relative to the case without a wind farm. The increase in TKE extended to the top of the BL above the farm due to vertical transport and wind shear, significantly enhancing turbulent momentum fluxes. Near the top of the BL, the TKE was increased by a factor of 2. The TKE also increased by a factor of 2 near the surface within the farm. This increase was responsible for accelerating the near-surface winds. The TKE source also led to a reduction of 25% in the wind speed deficit within the rotor area, compared to the case without any explicit source of TKE. In addition, the momentum deficit within the rotor area caused shear production of TKE above the rotor area. In the horizontal, an increase in TKE extended 10 km downstream at the hub-height level. Farther downstream, the TKE was reduced owing to the reduction in wind shear. More advection of TKE into the wake was seen at mid- to upper levels of the BL, where the dissipation was less and the wind speed greater.

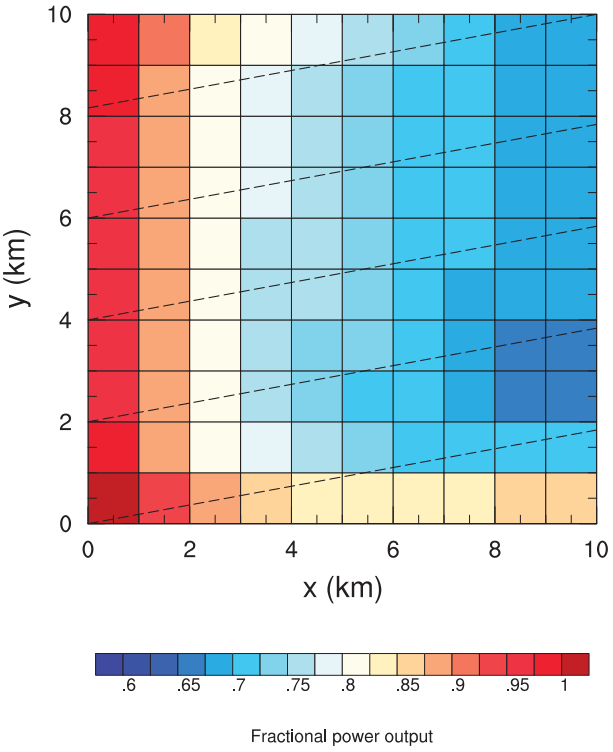

FIG. 12. Fractional power output for each turbine in each grid cell in the control (CTRL) simulation. The dashed lines indicate the direction of the west-southwesterly wind at hub height.

The downward flux of zonal momentum was enhanced within the wind farm area and above to the top of the BL by more than a factor of 5. Greater downward flux of zonal momentum also was seen at mid- to upper levels of the BL downwind of the farm, corresponding to regions where the wind shear and TKE were enhanced. Near the surface within the front side of the farm, the downward momentum flux was enhanced by nearly a factor of 2. However, near the surface in the rear end of the farm and wake, the flux was reduced by up to a factor of 1.3.

The sensitivity of the simulations to the magnitude of the TKE source was investigated, and was found to be small when considering the response within the rotor area and downstream in the neutral BL studied here. Within the rotor area, the uncertainty in wind speed was found to be 8% of the response to the wind farm in the control simulation (CTRL) when the TKE source was doubled or halved relative to CTRL. However, the magnitude of the TKE source was found to have a significant effect on near-surface winds within the wind farm, with an uncertainty of 40% of the response to CTRL. Downstream the uncertainty was a maximum of 18% of the response to CTRL. However, the uncertainty in the absolute value of the wind speed response was small, with a maximum of ± 0.2 m s^{-1} in the near-surface winds within the farm. Depending upon the application, these uncertainties are within acceptable limits. The uncertainty in near-surface winds is large when compared to the response in CTRL. When comparing surface momentum fluxes in different scenarios, this uncertainty should be considered. However, doubling or halving the TKE source represents an extreme range in values, which most likely will not be seen in practice if turbine mechanical and electrical losses are around 10%. Thus, the uncertainties are likely to be smaller than those given here.

The representation of TKE is improved further in the current work by including horizontal advection of TKE in the model. At higher resolutions, it becomes more important to advect TKE, where the TKE is able to persist to downstream grid cells before being dissipated. The pattern of TKE in the wake broadly agrees with the LES reported by Lu and Porté-Agel (2011) and wind-tunnel experiments reported by Chamorro and Porté-Agel (2009). Both found a decrease in turbulence in the lower region of the wake due to the reduction of wind shear, and greater turbulence above where the wind shear was increased. In addition, Chamorro and Porté-Agel (2009) found an increase in turbulence 15 rotor diameters downstream of a single turbine (corresponding to 1.9 km here). The regions of enhanced momentum fluxes also correspond well to those reported by Lu and Porté-Agel (2011), who found the momentum flux was greatest at the top of the turbines due to the enhanced mixing of momentum by the turbines in that region. In addition, the momentum flux was enhanced above hub height and decreased below. Calaf et al. (2010) and Lu and Porté-Agel (2011) calculated the ''effective'' momentum eddy diffusivity in their LES of a wind farm. The enhancement of eddy diffusivity associated with turbine mixing in the simulations reported here is similar to that found in their LES.

The wind turbine–induced forces are parameterized using the ''drag-disk'' model, without any representation of the forces that generate rotation in the turbine blades or the flow. Other models have used blade-element theory to calculate lift and drag forces, which induce rotation. However, in evaluating the two models, Wu and Porté-Agel (2011) found the mean velocity and turbulence were captured well using both models in the far-wake region in LES, when compared to measurements from wind-tunnel experiments. In the near-wake, rotation in the model was important. Porté-Agel et al. (2011) reported a similar conclusion. The far-wake region corresponds to a distance greater than 5 rotor diameters downstream, or 630 m in the simulations presented here. For applications where the grid size is greater than this distance, this implies the drag-disk model can adequately

capture the forcing; however, with finer horizontal resolutions, rotation in the model should be considered.

The atmospheric response to the wind farm will be dependent on wind speed. For the simulations presented here, we chose a wind speed in the region where turbine thrust and power coefficients are close to optimal. Thus, the results are indicative of the maximum response that would be seen. Future work will explore the sensitivity of the results to wind speed. In addition, the atmospheric stability in the BL will affect turbulent mixing mechanisms entraining higher momentum air at mid- and upper levels of the BL into the wind farm. The results presented here are for a neutral BL. One would expect the turbulent mixing to be suppressed in a stable atmosphere, leading to greater wind speed deficits within the farm and a wake extending for longer distances. On the other hand, in an unstable atmosphere, the opposite would be expected. The impact of stability on wind speed deficit and turbulent mixing will be studied in the future. When the BL is not neutral, it would also be of interest to explore the impact on heat fluxes in addition to momentum fluxes.

Few observations are available to verify the results presented here. The wind speed deficit in the wake compares well with observations from Christiansen and Hasager (2005), where an 8%–9% reduction (corresponding to an absolute reduction of 0.5–1.5 m s^{-1}) at a height of 10 m was seen immediately downstream of the Horns Rev and Nysted offshore wind farms in Denmark. However, these wind farms are somewhat smaller than that modeled here—the largest, Horns Rev, covers 19 km^2 and consists of 80 turbines of nominal power 2 MW. The wake was found not to recover over the 21-km distance studied with a neutral BL. Field experiments will need to be carried out to further develop models of wind farm–induced flow.

The parameterization is efficient enough, having little sensitivity to vertical and horizontal resolution, to be used in an idealized configuration in a global domain. Previous studies of the impacts of wind farms on global scales have parameterized turbines by increased surface roughness, neglecting any representation of turbulence or wind shear.

Acknowledgments. We wish to thank REpower for providing the thrust and power coefficients for the 5M turbine. We express our appreciation for research funding from a variety of sources. Funding for ACF is from NORCOWE; support for JKL and JM is from NREL LDRD 06501101. NREL is a national laboratory of the U.S. Department of Energy, Office of Energy Efficiency and Renewable Energy, operated by the Alliance for Sustainable Energy, LLC.

REFERENCES

Adams, A. S., and D. W. Keith, 2007: Wind energy and climate: modeling the atmospheric impacts of wind energy turbines. *Eos, Trans. Amer. Geophys. Union,* **88** (Fall Meeting Suppl.), Abstract B44B-08.

Baidya Roy, S., 2011: Simulating impacts of wind farms on local hydrometeorology. *J. Wind Eng. Ind. Aerodyn.,* **99,** 491–498, doi:10.1016/j.jweia.2010.12.013.

——, and J. J. Traiteur, 2010: Impacts of wind farms on surface air temperatures. *Proc. Natl. Acad. Sci. USA,* **107,** 17 899–17 904, doi:10.1073/pnas.1000493107.

——, S. W. Pacala, and R. L. Walko, 2004: Can large wind farms affect local meteorology? *J. Geophys. Res.,* **109,** D19101, doi:10.1029/2004JD004763.

Barrie, D. B., and D. B. Kirk-Davidoff, 2010: Weather response to a large wind turbine array. *Atmos. Chem. Phys.,* **10,** 769–775, doi:10.5194/acp-10-769-2010.

Barthelmie, R. J., and Coauthors, 2007: Modelling and measurements of wakes in large wind farms. *J. Phys.: Conf. Ser.,* **75,** 012049, doi:10.1088/1742-6596/75/1/012049.

——, and Coauthors, 2010: Quantifying the impact of wind turbine wakes on power output at offshore wind farms. *J. Atmos. Oceanic Technol.,* **27,** 1302–1317.

Blahak, U., B. Goretzki, and J. Meis, 2010: A simple parameterization of drag forces induced by large wind farms for numerical weather prediction models. *Proc. European Wind Energy Conf. and Exhibition 2010,* PO ID 445, Warsaw, Poland, EWEC, 186–189. [Available online at http://www.ewec2010proceedings.info/posters/PO.445_EWEC2010presentation.pdf.]

Cal, R. B., J. Lebrón, L. Castillo, H. S. Kang, and C. Meneveau, 2011: Experimental study of the horizontally averaged flow structure in a model wind-turbine array boundary layer. *J. Renewable Sustainable Energy,* **2,** 013106, doi:10.1063/1.3289735.

Calaf, M., C. Meneveau, and J. Meyers, 2010: Large eddy simulation study of fully developed wind-turbine array boundary layers. *Phys. Fluids,* **22,** 015110, doi:10.1063/1.3291077.

Chamorro, L. P., and F. Porté-Agel, 2009: A wind-tunnel investigation of wind-turbine wakes: Boundary-layer turbulence effects. *Bound.-Layer Meteor.,* **132,** 129–149, doi:10.1007/s10546-009-9380-8.

Charnock, H., 1955: Wind stress on a water surface. *Quart. J. Roy. Meteor. Soc.,* **81,** 639–640, doi:10.1002/qj.49708135027.

Christiansen, M. B., and C. B. Hasager, 2005: Wake effects of large offshore wind farms identified from satellite SAR. *Remote Sens. Environ.,* **98,** 251–268, doi:10.1016/j.rse.2005.07.009.

Dudhia, J., 2011: WRF version 3.3: New features and updates. *Proc. 12th Annual WRF Users' Workshop,* Boulder, CO, NCAR, 1.1.

Ivanova, L. A., and E. D. Nadyozhina, 2000: Numerical simulation of wind farm influence on wind flow. *Wind Eng.,* **24,** 257–269, doi:10.1260/0309524001495620.

Keith, D., J. DeCarolis, D. Denkenberger, D. Lenschow, S. Malyshev, S. Pacala, and P. J. Rasch, 2004: The influence of large-scale wind power on global climate. *Proc. Natl. Acad. Sci. USA,* **101,** 16 115–16 120, doi:10.1073/pnas.0406930101.

Kirk-Davidoff, D. B., and D. W. Keith, 2008: On the climate impact of surface roughness anomalies. *J. Atmos. Sci.,* **65,** 2215–2234.

Klemp, J. B., and R. B. Wilhelmson, 1978: The simulation of three-dimensional convective storm dynamics. *J. Atmos. Sci.,* **35,** 1070–1096.

Lu, H., and F. Porté-Agel, 2011: Large-eddy simulation of a very large wind farm in a stable atmospheric boundary layer. *Phys. Fluids,* **23,** 065101, doi:10.1063/1.3589857.

Mellor, G. L., and T. Yamada, 1974: A hierarchy of turbulence closure models for planetary boundary layers. *J. Atmos. Sci.,* **31,** 1791–1806.

——, and ——, 1982: Development of a turbulence closure model for geophysical fluid problems. *Rev. Geophys.,* **20,** 851–875, doi:10.1029/RG020i004p00851.

Nakanishi, M., and H. Niino, 2009: Development of an improved turbulence closure model for the atmospheric boundary layer. *J. Meteor. Soc. Japan,* **87,** 895–912, doi:10.2151/jmsj.87.895.

Porté-Agel, F., Y.-T. Wu, H. Lu, and R. J. Conzemius, 2011: Large-eddy simulation of atmospheric boundary layer flow through wind turbines and wind farms. *J. Wind Eng. Ind. Aerodyn.,* **99,** 154–168, doi:10.1016/j.jweia.2011.01.011.

Skamarock, W. C., and Coauthors, 2008: A description of the advanced research WRF version 3. NCAR Tech. Note NCAR/TN-475+STR, 125 pp.

Smith, S. D., 1988: Coefficients for sea surface wind stress, heat flux, and wind profiles as a function of wind speed and temperature. *J. Geophys. Res.,* **93** (C12), 15 467–15 472.

Wang, C., and R. G. Prinn, 2010: Potential climatic impacts and reliability of very large-scale wind farms. *Atmos. Chem. Phys.,* **10,** 2053–2061, doi:10.5194/acp-10-2053-2010.

——, and ——, 2011: Potential climatic impacts and reliability of large-scale offshore wind farms. *Environ. Res. Lett.,* **6,** 025101, doi:10.1088/1748-9326/6/2/025101.

Wu, Y.-T., and F. Porté-Agel, 2011: Large-eddy simulation of wind-turbine wakes: Evaluation of turbine parametrisations. *Bound.-Layer Meteor.,* **138,** 345–366, doi:10.1007/s10546-010-9569-x.

CORRIGENDUM

ANNA C. FITCH,* JOSEPH B. OLSON,+ JULIE K. LUNDQUIST,# JIMY DUDHIA,@
ALOK K. GUPTA,& JOHN MICHALAKES,** IDAR BARSTAD,& AND CRISTINA L. ARCHER++

* National Center for Atmospheric Research, Boulder, Colorado
+ NOAA/Earth System Research Laboratory, and Cooperative Institute for Research in Environmental Sciences, Boulder, Colorado
# Department of Atmospheric and Oceanic Sciences, University of Colorado, Boulder, and National Renewable Energy Laboratory, Golden, Colorado
@ Mesoscale and Microscale Meteorology Division, National Center for Atmospheric Research, Boulder, Colorado
& Uni Research, Bergen, Norway
** National Renewable Energy Laboratory, Golden, Colorado
++ College of Earth, Ocean, and Environment, University of Delaware, Newark, Delaware

(Manuscript received and in final form 12 November 2012)

In Fitch et al. (2012), it should be clarified that Eq. (12) defines the rate of change of turbulent kinetic energy (TKE) caused by the wind turbines, per unit mass of air, following convention. The units are $m^2\ s^{-3}$. Similarly, Eq. (11) defines the power output of the wind turbines per unit mass. When calculating the power output with the conventional units of kg $m^2\ s^{-3}$ (or W), Eq. (11) should be multiplied by the mass, resulting in the following:

$$P_{ijk} = \frac{1}{2} N_t^{ij} \Delta x \Delta y C_P \rho_{ijk} |\mathbf{V}|_{ijk}^3 A_{ijk}, \tag{1}$$

where P_{ijk} is the power output (W) in grid cell i, j, k; ρ_{ijk} is the air density; and Δx, Δy is the horizontal grid size in the zonal and meridional directions, respectively. The power coefficient of the turbines C_P is a function of the horizontal wind speed $|\mathbf{V}|_{ijk}$, and N_t is the number of turbines per square meter.

This equation was used when calculating the power output shown in Fig. 12 in Fitch et al. (2012). The code distributed with the Weather Research and Forecasting Model (WRF) (versions 3.3 and onward) is unaffected.

REFERENCE

Fitch, A. C., J. B. Olson, J. K. Lundquist, J. Dudhia, A. K. Gupta, J. Michalakes, and I. Barstad, 2012: Local and mesoscale impacts of wind farms as parameterized in a mesoscale NWP model. *Mon. Wea. Rev.,* **140,** 3017–3038.

Corresponding author address: Anna C. Fitch, National Center for Atmospheric Research, P.O. Box 3000, Boulder, CO 80307-3000.
E-mail: fitch@ucar.edu

DOI: 10.1175/MWR-D-12-00341.1